Chemical Engineering Journal 496 (2024) 154132

Contents lists available at ScienceDirect

Chemical Engineering Journal

journal homepage: www.elsevier.com/locate/cej

The entropy effect on the structure and microwave dielectric properties of high-entropy $Li_x(MgZnCoNi)_{(1\text{-}x)/4}Al_2O_{4\text{-}\delta}$ ceramics

Mingjun Xie [a], Yuanming Lai [a,*], Pingwen Xiang [a], Feng Liu [a], Linqiao Zhang [a], Xingyue Liao [a], Huan Huang [a], Qian Liu [a], Chongsheng Wu [a], Yuanxun Li [b]

[a] *School of Mechanical and Electrical Engineering, Chengdu University of Technology, Chengdu 610059, China*
[b] *State Key Laboratory of Electronic Thin Films and Integrated Devices, University of Electronic Science and Technology of China, Chengdu 610054, China*

ARTICLE INFO

Keywords:
High-entropy ceramics
High entropy effect
Microwave dielectric properties
Oxygen vacancy
Bond characteristics

ABSTRACT

In present study, high-entropy $Li_x(MgZnCoNi)_{(1\text{-}x)/4}Al_2O_{4\text{-}\delta}$ ceramics (x = 0.00–0.45) were synthesized using solid-state reaction route, which formed a single-phase spinel structure with a *Fd-3m* space group. The reduction in unit cell volume and lattice parameters were attributed to the compression of polyhedral structures. A moderate content of Li^+ ions promoted the grain growth and improved the densification of ceramics. The internal connection among the conformational entropy (ΔS_{config}), structure, and microwave dielectric properties in high-entropy $Li_x(MgZnCoNi)_{(1\text{-}x)/4}Al_2O_{4\text{-}\delta}$ ceramics was systematically studied. The dielectric constant (ε_r) was largely affected by the polarizability, and relatively high conformational entropy helped to increase the phonon vibrational energy and enhance the bond strength, resulting in low ε_r values. Additionally, the high concentration of oxygen vacancies, high packing fraction, low internal strain/fluctuation and suppressed damping behavior were closely related to relatively low conformational entropy. Notably, the introduction of oxygen vacancy leaded to the Al^{3+} ions preferentially occupy tetrahedral sites enhancing the covalency. These factors collectively reduced the intrinsic losses and improved the quality factor ($Q\times f$). Moreover, relatively high conformational entropy conduced to the structural stability by improving the M-O (M = Li, Mg, Zn, Co, and Ni) bond strength and valence, which contributes to achieve near-zero temperature coefficient of resonant frequency (τ_f). As ΔS_{config} changes, high-entropy $Li_x(MgZnCoNi)_{(1\text{-}x)/4}Al_2O_{4\text{-}\delta}$ ceramics presented great microwave dielectric properties: ε_r values of 5.46 ~ 8.49, $Q\times f$ values of 3,540 GHz (f = 14.84 GHz) ~ 56,950 GHz (f = 12.99 GHz), and τ_f values of −58 ppm/°C~ −14 ppm/°C. Our study demonstrates that the high-entropy strategy effectively enhances microwave dielectric properties. This approach has potential applications across a broad spectrum of microwave dielectrics ceramics.

1. Introduction

The rapid advancement of high-frequency communication has necessitated the development of 5G/6G communication equipment with enhanced capacity and faster transmission speeds, thereby more stringent performance requirements are proposed for microwave dielectric ceramics [1–4]. These ceramic materials, characterized by their appropriate dielectric constants (ε_r) and high quality-factor ($Q\times f$), play a vital role in contemporary communication systems, offering promising applications as filters, dielectric antennas, substrates, and resonators [5–7]. These materials also necessitate near-zero temperature coefficient of resonant frequency (τ_f), which makes them highly suitable for diverse electronic applications [8]. Notably, the dielectric materials with low ε_r value (below 10) can effectively minimize signal propagation delay [9]. High $Q\times f$ value ensure excellent frequency selectivity and energy efficiency [10]. While near-zero τ_f value guarantee thermal stability in communication devices [11]. Thus, the progression of advanced microwave dielectric ceramic is crucial in meeting the evolving demands.

In recent years, high-entropy alloys have attracted much attention for their excellent properties, including high hardness, fracture toughness, excellent thermal stability, and superionic conductivity [12–16], and have been widely applied to the modern industry. Moreover, the ongoing advancement of high-entropy alloys has sparked a keen interest in high-entropy ceramics [17–20]. High-entropy ceramics are characterized by a single-phase structure with a minimum of five major

---

* Corresponding author.
E-mail address: laiyuanming19@cdut.edu.cn (Y. Lai).

https://doi.org/10.1016/j.cej.2024.154132
Received 20 April 2024; Received in revised form 7 July 2024; Accepted 18 July 2024

elements in equal or nearly equal molar ratios, evenly dispersed throughout the cationic sublattice [14]. High-entropy ceramics exhibit four distinctive effects: high entropy effect, slow diffusion effect, lattice distortion effect, and cocktail effect [21,22]. Importantly, the high configurational entropy improves the solubility of multiple components simultaneously, enabling the optimization of specific properties [23]. This offers a novel and feasible strategy to modulate the properties of microwave dielectric materials.

It was discovered that high-entropy ceramics can be intentionally designed to have unique and stable structures by controlling configurational entropy (ΔS_{config}), which can be defined by Boltzmann's entropy equation [24,25]:

$$\Delta S_{config} = -R\sum_{i=1}^{N} x_i \ln x_i \tag{1}$$

where the R is the universal gas constant (8.314 J/mol·K) and the x_i is the molar content of the ith element. Evidently, adjusting the relative ratios of each constituent element will result in a change in ΔS_{config} within high-entropy ceramics. Recently, high-entropy ceramics with varied structures have been synthesized and subjected to comprehensive investigation owing to their promising microwave dielectric properties [26–28]. For instance, the high-entropy olivine-type $Li(Gd_{0.2}Ho_{0.2}Er_{0.2}Yb_{0.2}Lu_{0.2})GeO_4$ ceramics exhibited a near-zero τ_f value (–2.9 ppm/°C) [26]. The high-entropy spinel-type $(Mg_{0.2}Co_{0.2}Ni_{0.2}Li_{0.4}Zn_{0.2})Al_2O_4$ ceramics presented a high $Q\times f$ value (58,200 GHz) [27]. Notably, the high-entropy perovskite-type $SrLa(Al_{0.25}Zn_{0.125}Mg_{0.125}Ti_{0.25}Ga_{0.25})O_4$ ceramics presented a near-zero τ_f value (–1.7 ppm/°C) and a high $Q\times f$ value (83,003 GHz) [28]. Nevertheless, the configurational entropy in high-entropy ceramics that influence their microwave dielectric properties is not yet known. This study precisely focuses on the high-entropy strategy to modulate the microwave dielectric properties of spinel-type $MgAl_2O_4$ ceramics and investigates the potential effect of conformational entropy on microwave dielectric properties. The spinel-type oxides are more amenable to forming high-entropy oxides, owing to their two cationic sublattice sites [29]. Therefore, it would be more compelling to study the impact of ΔS_{config} in such complex structures, for establishing a better linkage among the ΔS_{config}, structure, and microwave dielectric properties.

In present study, for systematically investigating the internal connection among the ΔS_{config}, structure, and microwave dielectric properties, high-entropy $Li_x(MgZnCoNi)_{(1\text{-}x)/4}Al_2O_{4\text{-}\delta}$ ceramics (x = 0.00–0.45) were synthesized via solid-state reaction route. The crystal structure, lattice parameters, Raman vibrations, relative density, microstructure, polarizability, oxygen vacancy, packing fraction, internal strain/fluctuation, tolerance factor and chemical bond characteristics (bond strength, degree of covalency, and bond valence) of high-entropy $Li_x(MgZnCoNi)_{(1\text{-}x)/4}Al_2O_{4\text{-}\delta}$ ceramics were thoroughly investigated. These high-entropy research strategies and outcomes are anticipated to provide vital theoretical and pragmatic direction for the engineering of high-performance microwave dielectric ceramics, expected to contribute significantly to the advancement of the field.

2. Experimental procedure

The high-entropy $Li_x(MgZnCoNi)_{(1\text{-}x)/4}Al_2O_{4\text{-}\delta}$ ceramics (x = 0.00–0.45) were synthesized via solid-state reaction route. The raw materials, including analytically pure Li_2CO_3 (99%), MgO (98%), ZnO (99%), $CoCO_3$ (99%), $NiCO_3$ (99%), and Al_2O_3 (99%) powders (all obtained from Shanghai Macklin Biochemical Co. Ltd), were weighed according to the stoichiometric ratio in $Li_x(MgZnCoNi)_{(1\text{-}x)/4}Al_2O_{4\text{-}\delta}$. After ball-milling for 4 h in deionized water with zirconium balls, the mixed slurry was dried at 100 °C for 24 h. Then, the powders were pre-calcined at 1450 °C for 4 h. Next, the pre-calcined powders were ball-milled and dried again. Subsequently, the powders were mixed with PVA (10 wt%) and compressed into cylinders (the thickness and diameter are approximately 6 mm and 12 mm, respectively) under the pressure of 20 MPa. Finally, the cylinders were sintered at 1450–1600 °C for 4 h. Specific heating and cooling rates are detailed in the *Supplementary material*.

The bulk densities (ρ_{bulk}) of all samples were calculated by Archimedes' method (see *Supplementary material*). The phase composition and structure of the samples were analyzed using X-ray diffraction (XRD, Miniflex 600, Rigaku, Japan) ranging from 10° to 120° with Cu K_α radiation. The lattice parameters were obtained through refinements using the *Fullprof* software [30]. The lattice vibrations of the samples were explored through Raman spectra using Horiba Scientific LabRAM HR Evolution with λ = 738 nm. The morphology of the polished and thermally etched surfaces of the samples were examined using Scanning electron microscopy (SEM; JSM-6490, JEOL, Japan) at an accelerating voltage of 15 kV (thermal etching process is presented in *Supplementary material*). The mean grain size was quantified using *Nano Measure* software. The distribution of surface pores and Brunauer Emmett Teller (BET) specific surface area were detected by N_2 adsorption–desorption using the Micromeritics ASPS 2460 instrument. The elemental distribution of the x = 0.20 and 0.45 samples were verified using Energy dispersive X-ray spectroscopy (EDS). To determine the volatilization loss of Li^+ and Zn^{2+} ions during the sintering process, the composition of the x = 0.05, 0.25, and 0.45 samples were analyzed by the inductively coupled plasma spectroscopy (ICP-OES; Agilent 5110, USA). The elemental composition and oxygen vacancy were studied using X-ray photoelectron spectroscopy (XPS; ESCALAB 250Xi, Thermo Fisher, USA) with monochromatic Al K_α radiation and Electron paramagnetic resonance (EPR; X-band spectrometer E500, Bruker, German). The ε_r, $Q\times f$, and τ_f values of all samples were measured through the Hakki-Coleman dielectric resonator cavity method. Among them, the τ_f values were measured based on the resonance frequencies at 25 °C and 85 °C:

$$\tau_f = \frac{f(85^\circ C) - f(25^\circ C)}{(85-25)\times f(25^\circ C)} \times 10^6 (ppm/^\circ C) \tag{2}$$

3. Results and discussion

3.1. Phase composition and structure analysis

According to Boltzmann's entropy equation (see **Eq. (1)**), high-entropy ceramics are commonly defined as single-phase ceramics with high configurational entropy (≥ 1.5 R) [24,25]. The ΔS_{config} of the high-entropy $Li_x(MgZnCoNi)_{(1\text{-}x)/4}Al_2O_{4\text{-}\delta}$ ceramics (x = 0.00–0.45) are detailed in **Table S1**. With the x value rises, the ΔS_{config} of seven ceramic samples (x = 0.05–0.40) changes between 1.504 R and 1.609 R, which belongs to the category of high-entropy ceramics. The remaining x = 0.00 (ΔS_{config} = 1.386 R) and x = 0.45 (ΔS_{config} = 1.450 R) ceramic samples belong to medium-entropy ceramics. Moreover, the XRD patterns of high-entropy $Li_x(MgZnCoNi)_{(1\text{-}x)/4}Al_2O_{4\text{-}\delta}$ ceramics at 1600 ℃ are displayed in Fig. 1**(a)**. All high-entropy ceramic samples display similar XRD patterns and highly correspond with the spinel $MgAl_2O_4$ ceramics with *Fd-3m* space group (PDF No. #73–1959), which indicates that they are composed of the same substances [31]. Notably, all high-entropy $Li_x(MgZnCoNi)_{(1\text{-}x)/4}Al_2O_{4\text{-}\delta}$ ceramics form a single phase without any detectable secondary phase, suggesting that single-phase high-entropy $Li_x(MgZnCoNi)_{(1\text{-}x)/4}Al_2O_{4\text{-}\delta}$ ceramics have been successfully synthesized. The formation of the single phase can be attributed to the high entropy effect of ceramics. Thermodynamically, there is a correlation between entropy and enthalpy, which together determine the Gibbs free energy ($\Delta G = \Delta H - T\Delta S$, where ΔS is entropy, ΔH is enthalpy, and the T is temperature) [5,26]. As the ΔS increases, the Gibbs free energy decreases, implying that higher entropy will induce a more stable crystal structure. Thus, as the ΔS increases (≥ 1.5 R), the increase of $T\Delta S$ can overcome ΔH and make the Gibbs free energy negative to form a single phase (when T is high enough) [32]. Additionally, Fig. 1**(b)** demonstrates that the strongest diffraction

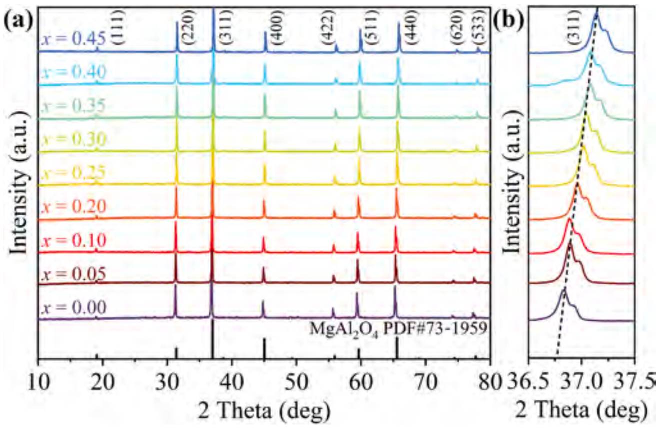

Fig. 1. XRD patterns of high-entropy $Li_x(MgZnCoNi)_{(1-x)/4}Al_2O_{4-\delta}$ ceramics sintered at 1600 ℃. (a) XRD patterns of high-entropy $Li_x(MgZnCoNi)_{(1-x)/4}Al_2O_{4-\delta}$ ceramics; (b) The enlarged XRD patterns.

characteristic peak (311 plane) moves towards higher angles with the rising *x* value, which is indicative of a narrower interplanar spacing. This can be ascribed to the reduction in cell volume originated from the lattice contraction [1].

For a more thorough examination of crystal structure and to obtain detailed lattice parameters of high-entropy $Li_x(MgZnCoNi)_{(1-x)/4}Al_2O_{4-\delta}$ ceramics. Rietveld refinement of the measured XRD data was carried out with *Fullprof* software [30]. Refined patterns of high-entropy $Li_x(MgZnCoNi)_{(1-x)/4}Al_2O_{4-\delta}$ ceramics are presented in Fig. 2**.** The Rietveld refinement results are listed in **Table S2**. The positions of Bragg reflections are in excellent agreement with the indexed peaks, and all fitted curves closely align with the measured data. Moreover, the smooth dark-colored error line ($Y_{obs} - Y_{cal}$) and the low goodness of fit indicator (χ^2) indicate the accuracy and reliability of Rietveld refinement results. Based on the refinement results, the crystal structure diagram of high-entropy $Li_x(MgZnCoNi)_{(1-x)/4}Al_2O_{4-\delta}$ ceramics is displayed in Fig. 2**(i)**, which comprises the [M/AlO$_4$] tetrahedra (M = Li, Mg, Zn, Co, and Ni) and [M/AlO$_6$] octahedra. In the crystal structure, the tetrahedron is connected to its neighboring octahedron by sharing vertices, whereas the octahedra are interconnected through their shared edges. Moreover,

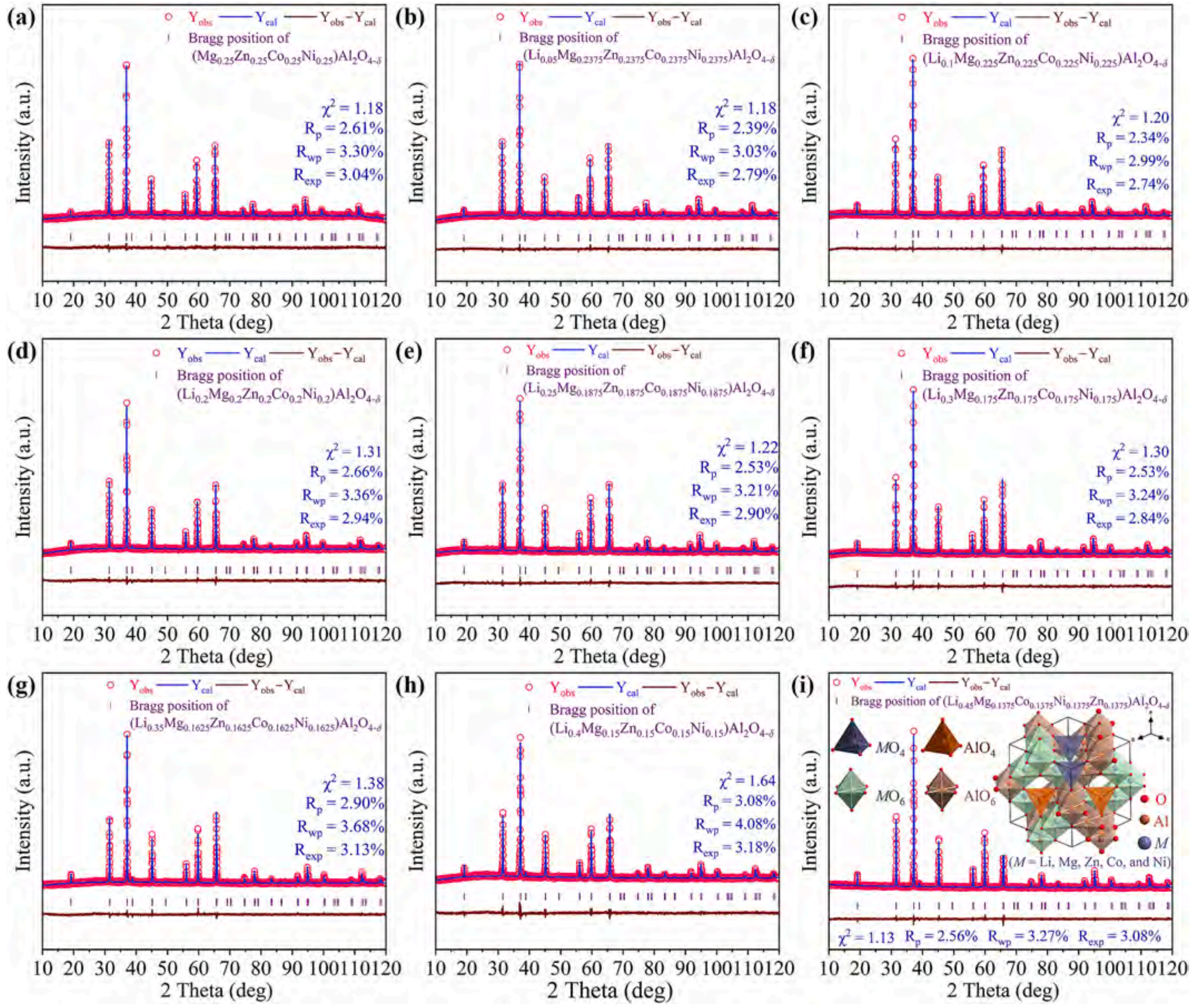

Fig. 2. Rietveld patterns and crystal structure of high-entropy $Li_x(MgZnCoNi)_{(1-x)/4}Al_2O_{4-\delta}$ ceramics sintered at 1600 ℃. (a) $x = 0.00$; (b) $x = 0.05$; (c) $x = 0.10$; (d) $x = 0.20$; (e) $x = 0.25$; (f) $x = 0.30$; (g) $x = 0.35$; (h) $x = 0.40$; (i) $x = 0.45$ and crystal structure diagram.

the tetrahedrons are not directly connected, but are instead connected via a common edge of the octahedrons. Notably, distortion and/or vibration within a tetrahedron and/or octahedron affect the structure, leading to variations in the unit cell volume and potentially affecting the properties.

The variation trend of the unit cell volume (V_{cell}) and lattice parameters (a, b, and c) in high-entropy $Li_x(MgZnCoNi)_{(1\text{-}x)/4}Al_2O_{4\text{-}\delta}$ ceramics are presented in Fig. 3. Both the cell volume and lattice parameters generally exhibit a decreasing trend as the x value rises (see Fig. 3**(a)-(b)**). Given that the M/Al-O bond presence also impacts the unit cell volume, to evaluate in-depth the influence of the bond length on crystal structure, the normalized bond length of M/Al-O bond in the [M/AlO_4] tetrahedron and [M/AlO_6] octahedron are displayed in Fig. 3 **(c)-(f)**. The normalized bond length reflects the state of the chemical bond. A normalized bond length less than 1 indicates that the bond is compressed, otherwise the bond is elongated [6,33]. Obviously, the M/Al-O bond in the [M/AlO_4] tetrahedron shows a progressively increasing compressed effect, while the M/Al-O bond in the [M/AlO_6] octahedron exhibits a gradually weakening compressed effect as the x value increases. Hence, the compression is the predominant factor influencing the crystal structure, and the reduction of unit cell volume and lattice parameters in high-entropy $Li_x(MgZnCoNi)_{(1\text{-}x)/4}Al_2O_{4\text{-}\delta}$ ceramics can be ascribed to the compression of [M/AlO_4] and/or [M/AlO_6] polyhedron [6].

3.2. Raman spectra analysis

Raman spectroscopy is a forceful approach for elucidating lattice vibrations. The Raman spectra of the high-entropy $Li_x(MgZnCoNi)_{(1\text{-}x)/4}Al_2O_{4\text{-}\delta}$ ceramics at 1600 ℃ are demonstrated in Fig. 4. Five Raman modes of spinel aluminates with *Fd-3m* space group have been predicted by group theory analysis as follows [34]:

$$\Gamma_{raman} = F_{2g}^{(1)} + F_{2g}^{(2)} + F_{2g}^{(3)} + E_g + A_{1g} \tag{3}$$

The Raman characteristic peaks have been allocated to various vibrational modes (see **Table S3**). However, not all Raman modes can be observed due to unavoidable factors, such as vibrational band broadening, and Raman peak overlap [35]. In present study, the $F_{2g}^{(1)}$ Raman mode located at about 185 cm^{-1} is presumed to the complete translation of the [MO_4] tetrahedra [34], the $F_{2g}^{(2)}$ Raman mode situated at about 535 cm^{-1} is assigned to the M-O stretching vibration within the [MO_4] tetrahedra [34,36], and the $F_{2g}^{(3)}$ Raman mode positioned at about 615 cm^{-1} is linked to the anti-symmetric stretching of the [M/AlO_4] tetrahedron and/or the asymmetric stretching of oxygen ions relative to the [M/AlO_4] tetrahedral cations [36,37]. Moreover, a strong association was observed between the tetrahedral cation radius and the Raman shift of the E_g Raman mode, the cation disordering can be inferred from the width and shape of the E_g Raman mode [34]. Thus, the E_g Raman mode placed at about 385 cm^{-1} is allocated to the asymmetric bending of the [MO_4] tetrahedron [38,39]. Notably, the A_{1g} Raman mode situated at about 765 cm^{-1} is ascribed to the symmetric Al-O stretching vibration of the [AlO_4] tetrahedra, which results from the redistribution of Al^{3+} ions from the octahedral sites to the tetrahedral sites [40]. This mode provides an intuitive and reliable basis for the occupation and redistribution of Al^{3+} on the tetrahedron [40,41].

Furthermore, the full width at half maximum (FWHM) of Raman peaks is closely linked to the cation disorder, and crystallinity within the ceramic structure [42]. The subtle Raman shifts and pronounced FWHM variations of the $F_{2g}^{(1)}$ and E_g Raman modes are observed in the enlarged Raman spectra (see Fig. 4**(b)**). The broadening of Raman peak (FWHM increases) is credited to the cation disorder, while the Raman shifts signifies the short-range order [34,42]. Additionally, for thoroughly examining the effect of crystal lattice vibrations on the properties, the fitted Raman spectra of the $x = 0.05$ and 0.10 samples depended on the Gauss/Lorentz function are illustrated in Fig. 4(c-d). The remaining sample's fitted Raman spectra are depicted in **Fig. S1**. The number of Raman peaks, which are fitted via the multi-peaks Gauss/Lorentz model, corresponds well to the theoretical values ($3F_{2g} + E_g + A_{1g}$). The impact

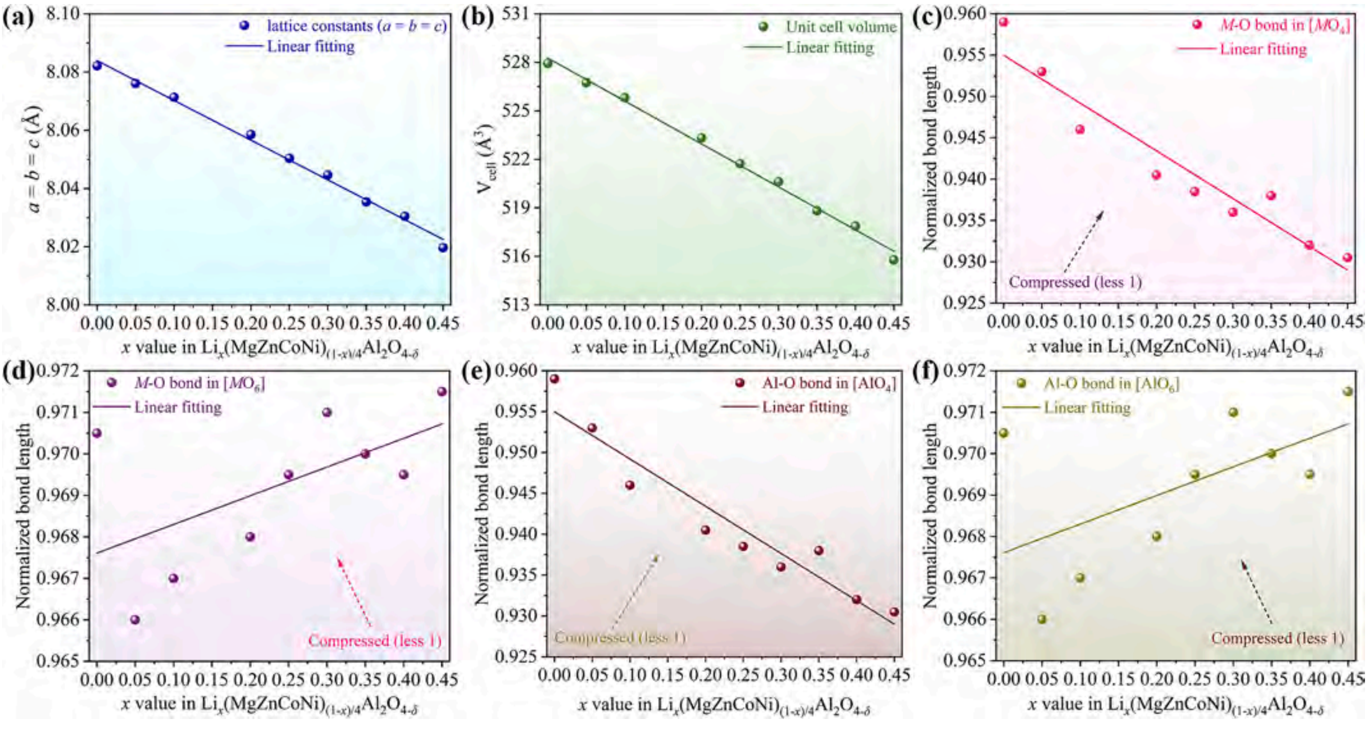

Fig. 3. The lattice parameters and unit cell volume of high-entropy $Li_x(MgZnCoNi)_{(1\text{-}x)/4}Al_2O_{4\text{-}\delta}$ ceramics sintered at 1600 ℃. (a)-(b) The variation trend of lattice parameters and unit cell volume; (c)-(d) The normalized bond length of M-O bond in the [MO_4] tetrahedron and [MO_6] octahedron; (e)-(f) The normalized bond length of Al-O bond in the [AlO_4] tetrahedron and [AlO_6] octahedron.

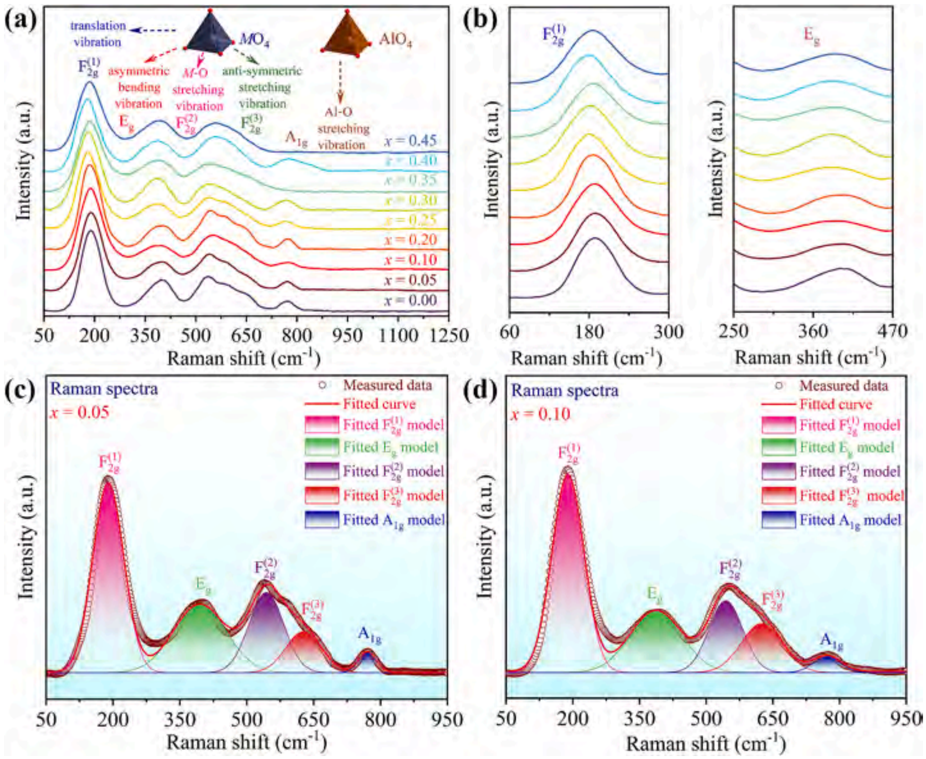

Fig. 4. Raman spectra of high-entropy $Li_x(MgZnCoNi)_{(1-x)/4}Al_2O_{4-\delta}$ ceramics sintered at 1600 ℃. (a) Raman spectra of all samples; (b) The enlarged Raman spectra peaks of the $F_{2g}^{(1)}$ and E_g modes; (c)-(d) Fitted Raman spectra curves of $x = 0.05$ and 0.10 samples.

of crystal lattice vibrations on the properties will be studied later.

3.3. Microstructure analysis

The SEM images of high-entropy $Li_x(MgZnCoNi)_{(1-x)/4}Al_2O_{4-\delta}$ ceramics ($x = 0.05$, 0.25, 0.35 and 0.45) at 1600 °C are presented in Fig. 5. The relative density of high-entropy $Li_x(MgZnCoNi)_{(1-x)/4}Al_2O_{4-\delta}$ ceramics gradually increases from 89.92% at $x = 0.00$ sample to 95.17% at $x = 0.45$ sample with the increasing Li^+ ion content (see **Table S2**). This can be attributed to that the Li^+ ion promote the sintering of ceramics and accelerate the elimination of pores [43]. Moreover, Fig. 5**(a)** illustrates that the $x = 0.05$ sample exhibits an abnormal grain growth and irregular grain distribution with clearly visible pores, matching with the lower relative density (90.53%). As Li^+ ion content increases, the mean grain size of the high-entropy ceramics noticeably enlarges (increases from 4.49 μm at $x = 0.05$ to 6.32 μm at $x = 0.45$) and the pores gradually diminish (see Fig. 5**(b)-(k)**). The microstructure of $x = 0.45$ samples exhibits excellent crystallization, with clearly visible grain boundaries and a uniform grain distribution, as well as desirable compactness (see Fig. 5**(a)-(j)**), which corresponds with the higher relative density (95.17%). This can be ascribed to that the increase in Li^+ ion promotes the mobility of grain boundaries [43]. Notably, the high temperature volatile diffusion of Li^+ ion can result in surface areas with increased grain boundary diffusion, thereby facilitating the grain growth and microstructure densification [27,39].

In order to study the microstructure of high-entropy $Li_x(MgZnCoNi)_{(1-x)/4}Al_2O_{4-\delta}$ ceramics in greater depth, the distribution of surface pores and BET specific surface area (S_{BET}) were detected. As illustrated in Fig. 5**(c)-(l)**, the total pore volume of high-entropy $Li_x(MgZnCoNi)_{(1-x)/4}Al_2O_{4-\delta}$ ceramics decreases from 0.00497 cm^3/g at $x = 0.05$ to 0.00075 cm^3/g at $x = 0.45$, which corresponds well with a gradual increase in relative density, and the average pore diameter of the ceramic samples also decreases from 205.944 nm at $x = 0.05$ to 79.506 nm at $x = 0.45$, which can be attributed to the increase of Li^+ ions contributes to grain growth and the densification of the microstructure. The $x = 0.35$ sample has the smallest average pore diameter, which is consistent with its dense microstructure and the absence of significant pores (see Fig. 5 **(g)**). Moreover, the S_{BET} value of $x = 0.05$, 0.25, and 0.35 samples (0.0376 m^2/g, 0.0966 m^2/g, and 0.159 m^2/g, respectively) are lower than the $x = 0.45$ sample (0.621 m^2/g), this is due to the microstructure of the $x = 0.45$ sample with uniform grain growth, clear grain boundaries and good crystallinity.

To delve into the phase composition and evaluate the uniformity of element distribution, the EDS mappings analysis of the $x = 0.20$ and 0.45 samples in high-entropy $Li_x(MgZnCoNi)_{(1-x)/4}Al_2O_{4-\delta}$ ceramics was implemented and presented in Fig. 6. The distributions of the Al, O and *M*-site elements (Li is undetectable by EDS) are well-proportioned without any aggregation (the similar distribution for $x = 0.20$ sample is presented in **Fig. S2**, see ***Supplementary Material***), confirming the elemental regularity of the high-entropy ceramics [44]. Moreover, the atomic ratios of each element are exhibited in Fig. 6. The content of the *M*-site elements is found to be approximately equimolar ratios (except for Li). In addition, the mole ratios of the Al, O and *M*-site elements highly coincide with the stoichiometry of AB_2O_4. All results verify the chemical homogeneity of high-entropy $Li_x(MgZnCoNi)_{(1-x)/4}Al_2O_{4-\delta}$ ceramics and correspond well to the XRD analysis.

Since Li element is undetectable by EDS-mapping analysis, in addition, considering that Li^+ and Zn^{2+} ions are easy to volatilize at high temperature, the ICP-OES analysis were performed to accurately determine the amounts of Li^+ and Zn^{2+} in high-entropy $Li_x(MgZnCoNi)_{(1-x)/4}Al_2O_{4-\delta}$ ceramic samples. The results of ICP-OES analysis show that the Li contents in the $x = 0.05$, 0.25, and 0.45 samples are 0.09%, 0.39% and 0.83%, and the Zn contents are 2.73%, 2.84% and 2.62%, respectively, the actual contents of Li and Zn elements are lower than the theoretical values (see **Table S4**). The results indicate that the Li^+ and Zn^{2+} ions volatilize nearly 50% during the sintering process.

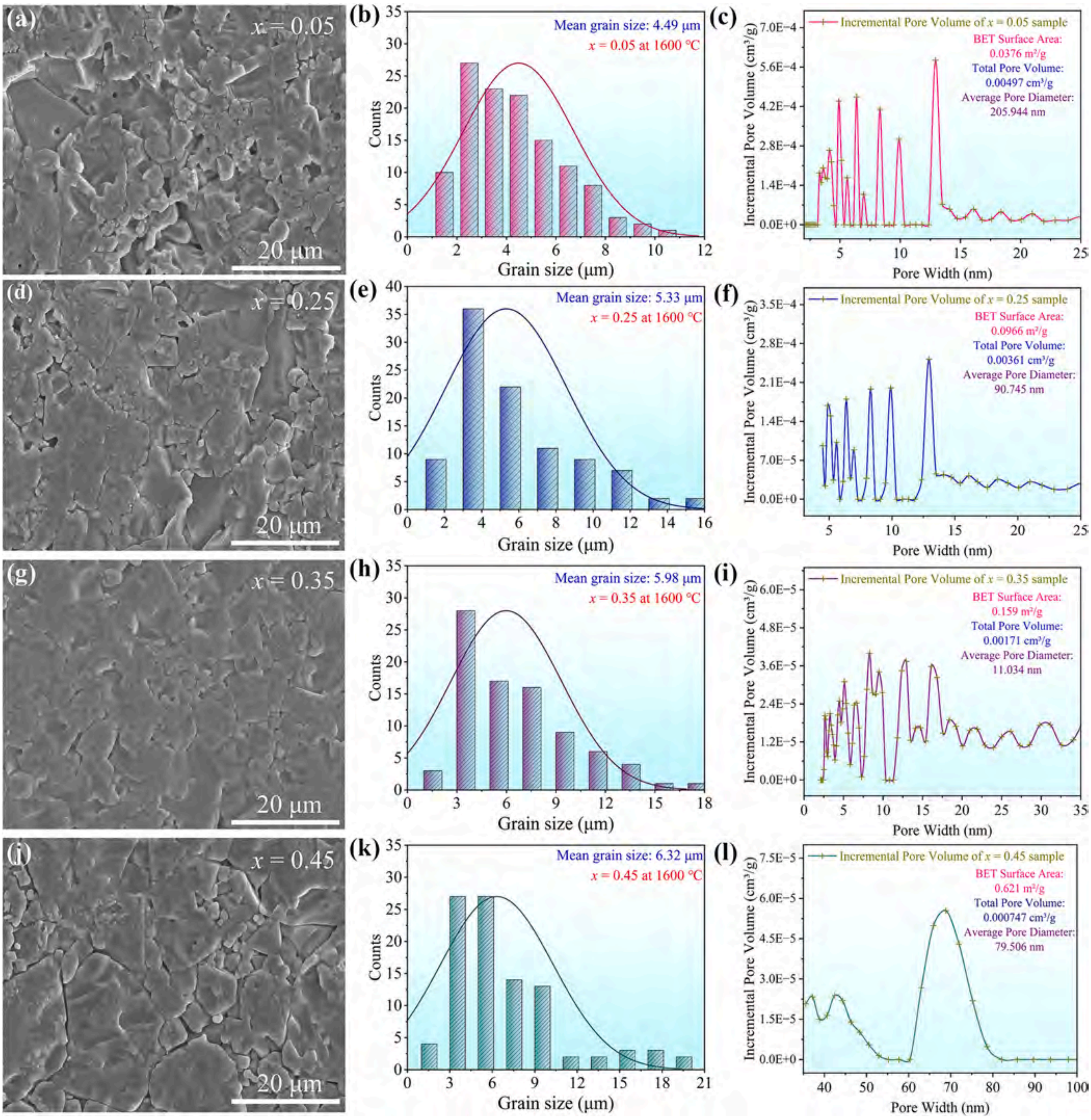

Fig. 5. The SEM images, mean grain size, and pore volume of high-entropy $Li_x(MgZnCoNi)_{(1-x)/4}Al_2O_{4-\delta}$ ceramics sintered at 1600 ℃: (a)-(c) The $x = 0.05$ sample; (d)-(f) The $x = 0.25$ sample; (g)-(i) The $x = 0.35$ sample; (j)-(l) The $x = 0.45$ sample.

3.4. Microwave dielectric properties

The microwave dielectric properties of high-entropy $Li_x(MgZnCoNi)_{(1-x)/4}Al_2O_{4-\delta}$ ceramics under different x value are displayed in Fig. 7 **(a)-(c)**. The ε_r values remain between 5.46 and 8.49, and gradually increase with the increasing x value (see Fig. 7**(a)**). The $Q\times f$ value also shows an overall increasing trend with the rise of x value and achieves its maximum value of 56,950 GHz ($f = 12.99$ GHz) at $x = 0.40$ (see Fig. 7 **(b)**). In addition, as the x value increases, the τ_f value first shows an increasing trend and achieves a relatively near-zero τ_f value (−14 ppm/°C) for $x = 0.05$ samples at 1450 ℃. And then, with the x value continues to increase, the overall τ_f value shows a gradual decreasing trend (see Fig. 7**(c)**). As illustrated in Fig. 7 (d), with the sintering temperature increases, the $Q\times f$ value gradually increases. Notably, as the sintering temperature further increases, the $Q\times f$ value of some samples shows a downward trend. This is because a higher sintering temperature can promote grain growth and increase the densification of the ceramic system [45]. However, excessive sintering temperature will deteriorate the microstructure of the ceramic system, which reduces the $Q\times f$ value.

Fig. 7**(e)-(g)** demonstrates the connection between the ΔS_{config} and microwave dielectric properties of high-entropy $Li_x(MgZnCoNi)_{(1-x)/4}Al_2O_{4-\delta}$ ceramics with different sintering temperature. Specifically, when the ΔS_{config} is a constant, the ε_r, $Q\times f$ and τ_f values of high-entropy $Li_x(MgZnCoNi)_{(1-x)/4}Al_2O_{4-\delta}$ ceramics gradually increase with the

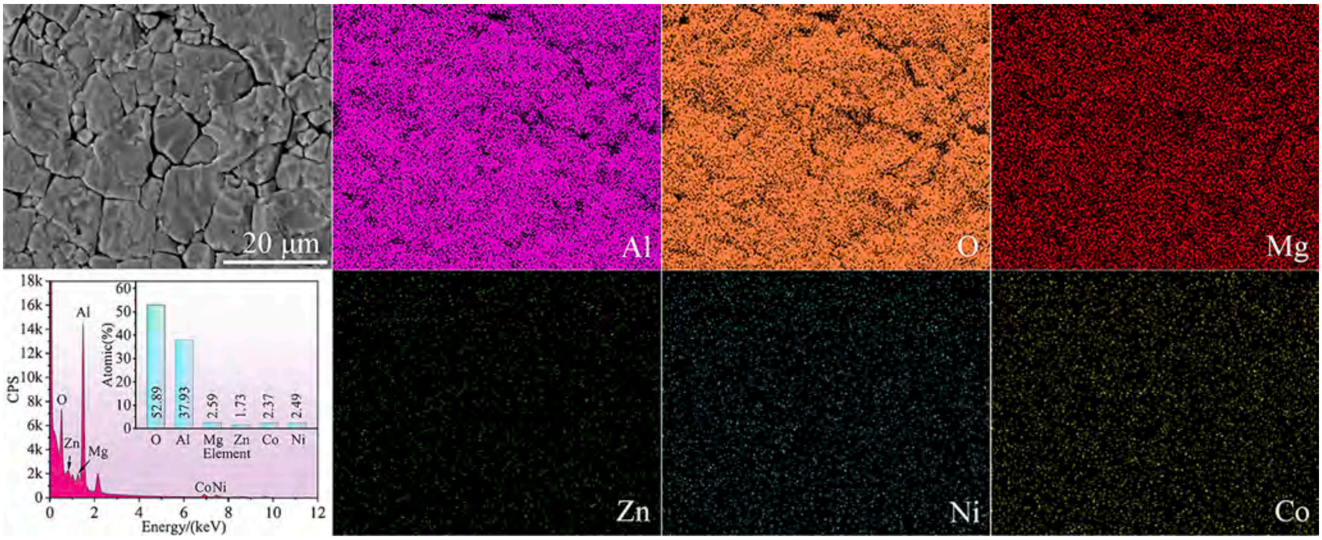

Fig. 6. The EDS mappings of high-entropy $Li_x(MgZnCoNi)_{(1-x)/4}Al_2O_{4-\delta}$ ceramics for $x = 0.45$ sample sintered at 1600 ℃ for 4 h.

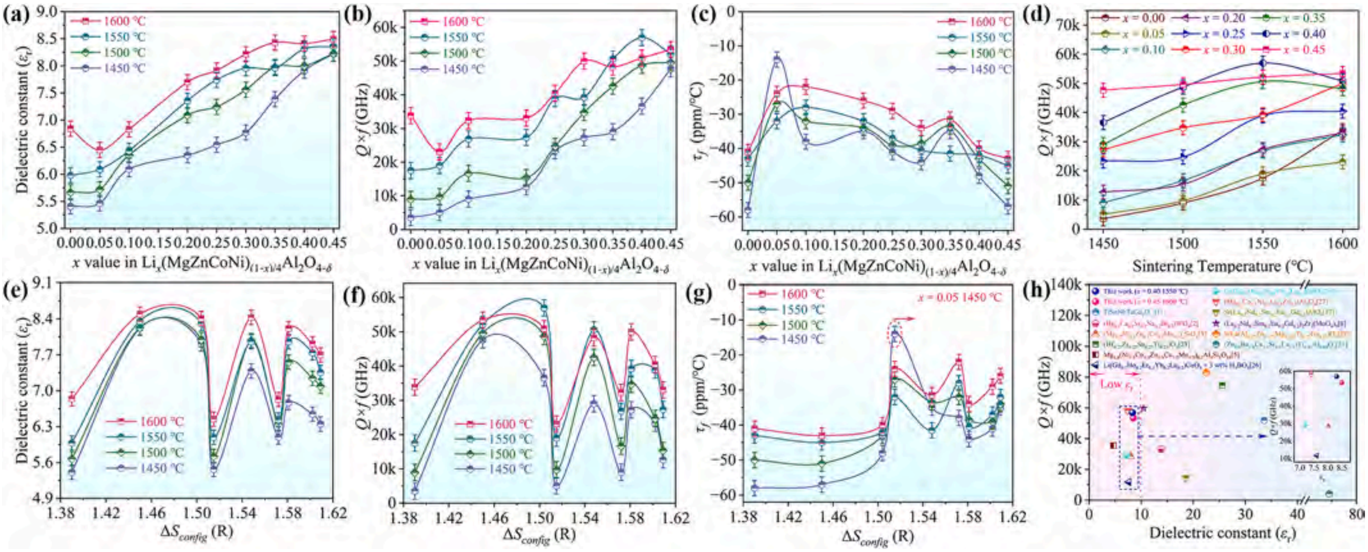

Fig. 7. Microwave dielectric properties of high-entropy $Li_x(MgZnCoNi)_{(1-x)/4}Al_2O_{4-\delta}$ ceramics. (a) The ε_r values under different x value; (b) The $Q\times f$ values under different x value; (c) The τ_f values under different x value; (d) The $Q\times f$ values under different sintering temperature; (e) The ε_r values under different ΔS_{config}; (f) The $Q\times f$ values under different ΔS_{config}; (g) The τ_f values under different ΔS_{config}; (h) Summary of $Q\times f$ values versus ε_r values of high-entropy microwave dielectric ceramics.

increase of sintering temperature, this can be attributed to that higher sintering temperatures can promote grain growth, resulting in a relatively uniform grain distribution and dense microstructure in ceramic samples [45,46]. Additionally, when the sintering temperature is a constant, the ε_r and $Q\times f$ values show an overall decreasing trend with the ΔS_{config} increase from 1.450 R to 1.609 R, while the τ_f values show an increasing trend with the ΔS_{config} increase from 1.386 R to 1.609 R. This indicates that there is a strong intrinsic correlation between the ΔS_{config} and microwave dielectric properties of high-entropy $Li_x(MgZnCoNi)_{(1-x)/4}Al_2O_{4-\delta}$ ceramics. Moreover, Fig. 7**(h)** reveals a summary of the $Q\times f$ value versus ε_r value between the present study and other high-entropy microwave dielectric ceramics. In comparison to other high-entropy ceramics, a higher $Q\times f$ value 56,950 GHz ($f = 12.99$ GHz) is achieved for $x = 0.40$ sample, while possessing a low ε_r value ($\varepsilon_r = 8.3$). In addition, compared with some of the $MgAl_2O_4$-based ceramics (see **Fig. S3** in *Supplementary Material*), the $x = 0.40$ and 0.45 samples of high-entropy $Li_x(MgZnCoNi)_{(1-x)/4}Al_2O_{4-\delta}$ ceramics present high $Q\times f$ value of 56,950 GHz ($f = 12.99$ GHz) and 53,400 GHz ($f = 13.17$ GHz), respectively. Importantly, the $x = 0.40$ and 0.45 samples improve the $Q\times f$ value of $MgAl_2O_4$ ceramics (~42,000 GHz) by nearly 13,000 GHz [45].

3.4.1. Dielectric constant (ε_r)

Fig. 8 displays the trend of ε_r values with ΔS_{config} at 1600 °C in high-entropy $Li_x(MgZnCoNi)_{(1-x)/4}Al_2O_{4-\delta}$ ceramics. Obviously, the ε_r values overall decreases from 8.49 at 1.450 R to 7.69 at 1.609 R, which suggests a strong relationship between the ε_r value and the ΔS_{config}. Generally, the ε_r value is chiefly dictated by ionic polarizability and is influenced by other factors, such as the densification, phonon vibration, and rattling effect [47,48]. Based on Clausius–Mosotti equation, the theoretical dielectric constant (α_{theo}) can be calculated [49]:

$$\varepsilon_{theo} = \frac{3V_m + 8\pi\alpha_D}{3V_m - 4\pi\alpha_D} \tag{4}$$

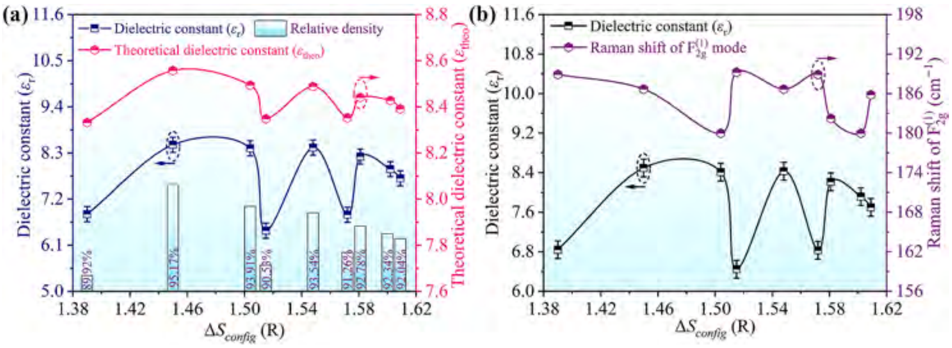

Fig. 8. The ε_r, ε_{theo} and relative density of high-entropy $Li_x(MgZnCoNi)_{(1-x)/4}Al_2O_{4-\delta}$ ceramics sintered at 1600 ℃. (a) The ε_r values, ε_{theo} values and relative density; (b) The ε_r value and Raman shift of the $F_{2g}^{(1)}$ phonon mode.

where the V_m is the molar volume of high-entropy $Li_x(MgZnCoNi)_{(1-x)/4}Al_2O_{4-\delta}$ ceramics. According to Shannon's addition rule, the α_D is achieved from the polarizability of all the constituent ions [49]:

$$\begin{aligned}\alpha_D &= \alpha\left[Li_x(MgZnCoNi)_{(1-x)/4}Al_2O_4\right]\\ &= (1-x)\left[\alpha(Mg^{2+})+\alpha(Zn^{2+})+\alpha(Co^{2+})+\alpha(Ni^{2+})\right]/4\\ &\quad +x\alpha(Li^{+})+2\alpha(Al^{3+})+4\alpha(O^{2-})\end{aligned} \tag{5}$$

where $\alpha(Li^+)$, $\alpha(Mg^{2+})$, $\alpha(Zn^{2+})$, $\alpha(Co^{2+})$, $\alpha(Ni^{2+})$, $\alpha(Al^{3+})$, and $\alpha(O^{2-})$ represent the ionic polarizabilities of Li^+(1.20 Å^3), Mg^{2+}(1.32 Å^3), Zn^{2+}(2.04 Å^3), Co^{2+}(1.65 Å^3), Ni^{2+}(1.32 Å^3), Al^{3+}(0.79 Å^3), and O^{2-}(2.01 Å^3), respectively [49]. The calculated ε_{theo} values are exhibited in **Table S5**. The trend of the ε_r value corresponds well to that of the ε_{theo} value (see Fig. 8**(a)**), indicating that the polarizability is a major factor dominating the ε_r value. Hence, the lower ε_r value of $x = 0.05$ samples ($\varepsilon_r = 6.45$) can be ascribed to the lower ionic polarizability. Furthermore, the ε_r values are closely aligned with the relative density in present study (see Fig. 8**(a)**).

Additionally, the Raman shift is affected by changes in electron density [50]. Thus, it is closely linked to the polarizability. The correlation between the Raman shift and the ε_r value is expressed as follows [51]:

$$\varepsilon_r(0,\xi,s) = \frac{\Omega_p^2 \exp\left(\lambda\left(E_F^0-\xi\right)\right)}{\omega(\xi,s)} \tag{6}$$

where the ξ, ω and Ω_p denotes the ionization energy, phonon frequency and plasma frequency, respectively. The E_F^0 represents the Fermi level at T = 0. As stated in **Eq.** (6), the Raman shift is inversely correlated with the ε_r value. The Raman shift of the $F_{2g}^{(1)}$ phonon mode (at 185 cm^{-1}) in high-entropy $Li_x(MgZnCoNi)_{(1-x)/4}Al_2O_{4-\delta}$ ceramics is exhibited in Fig. 8 **(b)**. The blue shift suggests an increase in the vibrational energy of the phonon vibrational mode, which corresponds to a weakening of the polarizability and an enhance in the bond strength, leading to a reduction in the ε_r value [52]. Whereas the red shift is exactly opposite of the blue shift. The Raman shift of the $F_{2g}^{(1)}$ phonon mode exhibits an opposite trend to the ε_r value as ΔS_{config} varies, corresponding to **Eq.** (6). Therefore, the conformational entropy affects the phonon vibrations of the Raman peaks and consequently leads to changes in the bond strength as well as polarizabilities, which significantly influence the ε_r values. The results confirm that the ε_r value of high-entropy $Li_x(MgZnCoNi)_{(1-x)/4}Al_2O_{4-\delta}$ ceramics highly relies on the polarizability, densification and conformational entropy.

3.4.2. Quality factor (Q×f)

Fig. 7 presents the trend of the $Q\times f$ value varied with the ΔS_{config} in high-entropy $Li_x(MgZnCoNi)_{(1-x)/4}Al_2O_{4-\delta}$ ceramics at 1600 °C. Clearly, the $Q\times f$ values decrease from 53,400 GHz ($f = 13.17$ GHz) at 1.450 R to 33,060 GHz ($f = 12.92$ GHz) at 1.609 R, which suggests that the $Q\times f$ value is closely associated with the ΔS_{config}. To further explore the inherent correlation between the $Q\times f$ and ΔS_{config} in high-entropy $Li_x(MgZnCoNi)_{(1-x)/4}Al_2O_{4-\delta}$ ceramics, it is requisite to delve into the effects of intrinsic and extrinsic losses on the $Q\times f$. Commonly, extrinsic losses comprise the porosity, crystallinity, and densification [53], whereas intrinsic losses contain bond characteristics, oxygen vacancy, packing fraction, lattice vibration, and internal fluctuation/strain [45,54].

Notably, the increase in the $Q\times f$ value can be attributed to the significant role of acceptor Li^+ ion in high-entropy $Li_x(MgZnCoNi)_{(1-x)/4}Al_2O_{4-\delta}$ ceramics. Due to the presence of acceptor Li^+ ions with low valency, and the Li^+ ions are partially volatilized during the sintering process, thus the ceramic system inevitably will generate oxygen vacancies to maintain charge neutrality [55,56]. The oxygen vacancy mechanism can be elucidated as follows [57]:

$$2Li^{+} + M^{2+} \rightarrow 2Li_{M}^{'} + V_{O}^{\cdot\cdot} \tag{7}$$

The creation of oxygen vacancies implies that the defect is introduced into the high-entropy ceramics. For characterizing the chemical composition and exploring the mechanism of oxygen vacancy defects effect on the $Q\times f$, the XPS spectra of high-entropy $Li_x(MgZnCoNi)_{(1-x)/4}Al_2O_{4-\delta}$ ceramics are display in Fig. 9.

The XPS spectra of high-entropy $Li_x(MgZnCoNi)_{(1-x)/4}Al_2O_{4-\delta}$ ceramic samples were calibrated against the C 1s peak at 284.8 eV. As illustrated in Fig. 9**(a)**, the C 1s, O 1s, Mg 1s, Zn 2p, Co 2p, Ni 2p, and Al 2p peaks are clearly observed over the survey XPS spectra of $x = 0.05$, 0.25 and 0.45 samples, which also implies the existence of Mg, Zn, Co, Ni, Al, and O elements in the high-entropy $Li_x(MgZnCoNi)_{(1-x)/4}Al_2O_{4-\delta}$ ceramics [58]. Notably, the high-resolution XPS spectra peak located at about 60.8 eV in Fig. 9**(b)-(d)** is nominated as Li 1s, which also confirms the existence of element Li in the high-entropy ceramics that undetectable by EDS-mapping analysis. Moreover, the high-resolution XPS spectra of O 1s in high-entropy $Li_x(MgZnCoNi)_{(1-x)/4}Al_2O_{4-\delta}$ ceramics are demonstrated in Fig. 9**(e)-(g)**. For examining the content of oxygen vacancies, the fitted curves of the O 1s XPS spectra are obtained using *avantage* software, which align well with the Gaussian subpeaks. The peaks centered at about 529.2 eV and 530.3 eV are attributed to the lattice oxygen and oxygen vacancies, respectively [59,60]. Whereas the peak situated at about 531.4 eV is ascribed to the oxide in hydroxide originated from O_2 and/or H_2O absorbed on the surface of high-entropy $Li_x(MgZnCoNi)_{(1-x)/4}Al_2O_{4-\delta}$ ceramics [61]. In present study, the proportion of the $V_{O}^{\cdot\cdot}$ area to the O 1s area is employed to determine the oxygen vacancy content [52], as detailed in **Table S6**. Obviously, the oxygen vacancies rise from 42.84% at $x = 0.05$ to 56.28% at $x = 0.45$ with the increasing Li^+ ion, suggesting that a higher concentration of acceptors enhances the oxygen vacancies in the lattice structure.

Moreover, the EPR analysis serves as an effective means for identifying ions containing unpaired electrons within ceramic materials. In

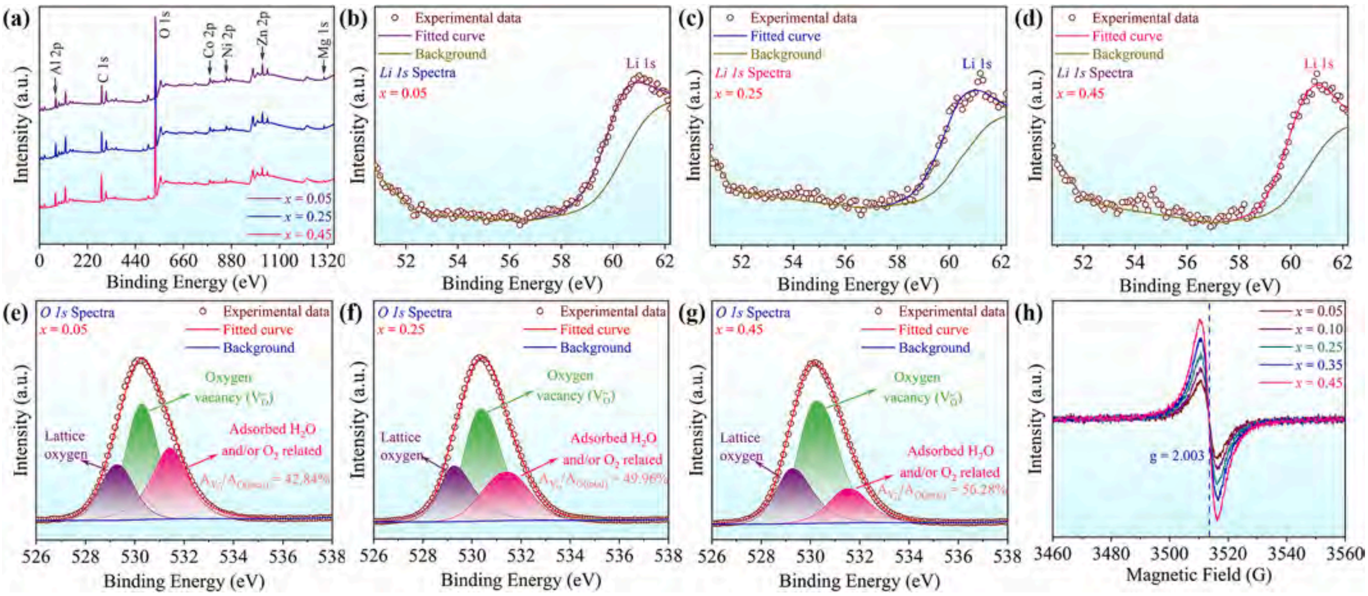

Fig. 9. The XPS and EPR spectra of high-entropy $Li_x(MgZnCoNi)_{(1-x)/4}Al_2O_{4-\delta}$ ceramics sintered at 1600 °C. (a) The survey XPS spectra of the high-entropy ceramic for $x = 0.05$, 0.25 and 0.45 samples; (b)-(d) The high-resolution XPS spectra of Li 1s for $x = 0.05$, 0.25 and 0.45 samples; (e)-(g) The high-resolution XPS spectra of O 1s for $x = 0.05$, 0.25 and 0.45 samples; (h) The room temperature EPR spectra of $x = 0.05$, 0.10, 0.25, 0.35 and 0.45 samples.

present study, EPR is also employed to evaluate the presence of oxygen vacancy [62]. Fig. 9**(h)** reveals the room temperature EPR spectra of high-entropy $Li_x(MgZnCoNi)_{(1-x)/4}Al_2O_{4-\delta}$ ceramics ($x = 0.05$, 0.10, 0.25, 0.35 and 0.45). The signal at $g = 2.003$ is the result of electrons being captured by oxygen vacancies [57,62]. Notably, the peak intensity of the EPR signal at $g = 2.003$ gradually increases, which implies that

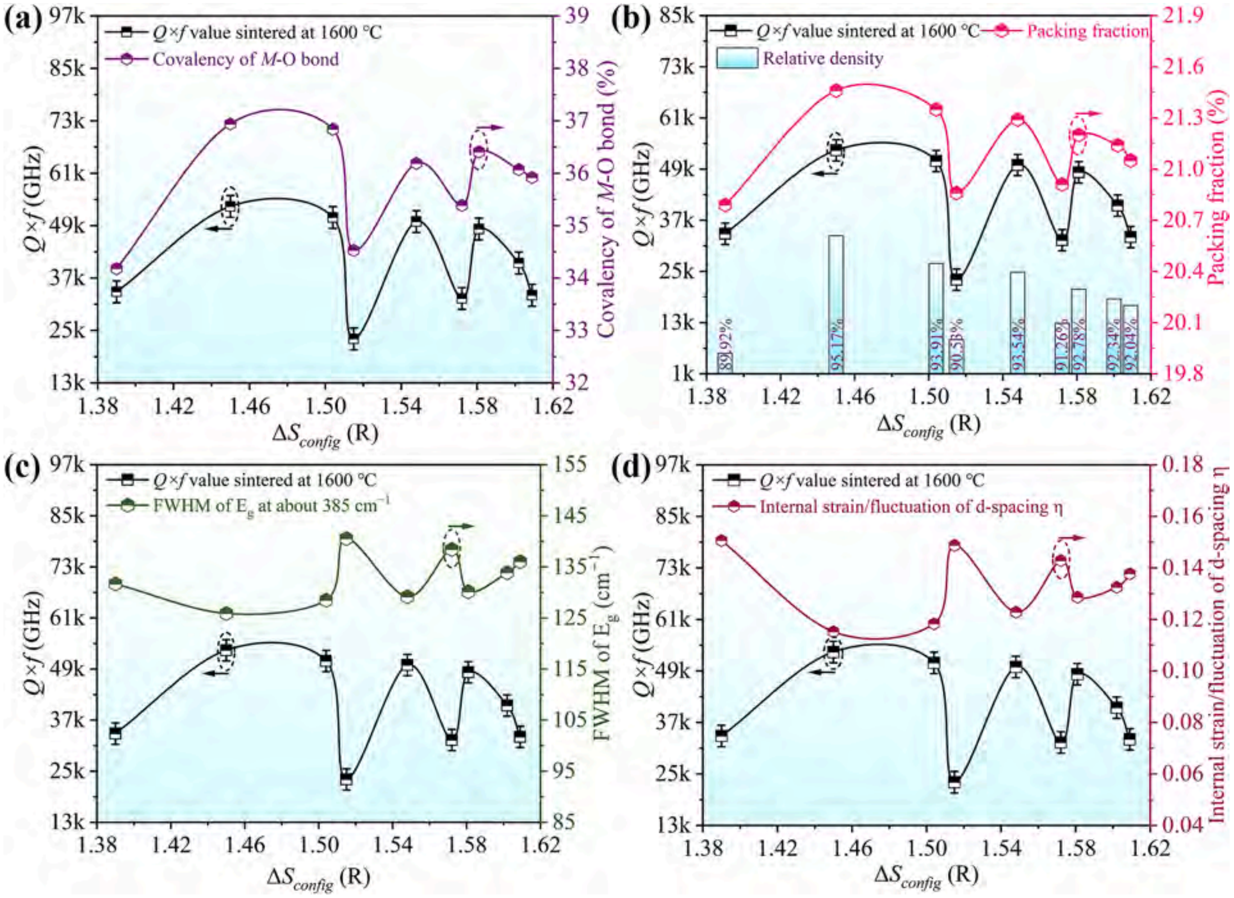

Fig. 10. The $Q\times f$ values, degree of covalency for M-O bond, packing fraction, relative density, FWHM of E_g mode and internal strain/fluctuation of high-entropy $Li_x(MgZnCoNi)_{(1-x)/4}Al_2O_{4-\delta}$ ceramics sintered at 1600 ℃. (a) The $Q\times f$ values and degree of covalency of M-O bond; (b) The $Q\times f$ values and packing fraction; (c) The $Q\times f$ values and FWHM of E_g mode; (d) The $Q\times f$ values and internal strain/fluctuation of d-spacing.

more oxygen vacancies are generated with the increasing Li^+ ion content. This is well coherent with the XPS analysis.

The XPS and EPR analyses manifest that more oxygen vacancies are generated as the acceptor Li^+ ion increases, which also significantly improves the $Q \times f$ value. Notably, the improvement mechanism of the $Q \times f$ value by oxygen vacancies can be ascribed to the Al^{3+} ions preferentially occupy the tetrahedral sites, which has been confirmed by previous studies [39,41,63]. To examine in-depth whether the improvement of $Q \times f$ value by oxygen vacancies is intrinsically linked to the Al^{3+} ions preferentially occupy the tetrahedral sites, the degree of covalency based on the covalence (f_c) and bond strength (s) in [MO_4] tetrahedron and [MO_6] octahedron is calculated [63–65]:

$$s = \left(\frac{R_{avg}}{R_1}\right)^{-N} \tag{8}$$

$$f_c = a \times s^M \tag{9}$$

$$\text{the degree of covalency } (\%) = \left(\frac{f_c}{s}\right) \times 100\% \tag{10}$$

where the R_{avg} denotes the average M-O bond length in [MO_4] tetrahedra or [MO_6] octahedron, the N and R_1 represent the empirical constants that hinge on the cation site and cation–anion pair [64]. Additionally, the M and a are the empirical parameters depending on the number of electrons [65]. The degree of covalency for M-O bond in [MO_4] tetrahedra and [MO_6] octahedra are detailed in **Tables S7 and S8**. Fig. 10**(a)** demonstrates the degree of covalency for M-O bond in the [MO_4] tetrahedron, which increases from 34.08% at 1.386 R to 36.94% at 1.450 R, corresponding well with the trend of the $Q \times f$ values. Meanwhile, the degree of covalency for M-O bond in the [MO_6] tetrahedra slightly decreases from 33.47% at 1.515 R to 32.97% at 1.450 R (see **Table S8**). The results confirm that the presence of oxygen vacancy facilitates the Al^{3+} ions to preferentially occupy [MO_4] tetrahedral sites. This enhances the degree of covalency for M-O bond in [MO_4] tetrahedron, thereby reducing the intrinsic loss of the ceramic material and increasing the $Q \times f$ value.

The $Q \times f$ value of high-entropy $Li_x(MgZnCoNi)_{(1-x)/4}Al_2O_{4-\delta}$ ceramics varies with the ΔS_{config}, indicating that the $Q \times f$ value is significantly affected by the ΔS_{config}. Notably, packing fraction reflects the structural loss originated from nonharmonic vibration [66]. Therefore, the inherent connection among the ΔS_{config}, structure, and $Q \times f$ values can be evaluated by packing fraction [66,67]:

$$packing\ fraction = \frac{4\pi \times \left[xR_{Li}^3 + (1-x)\left(R_{Mg}^3 + R_{Zn}^3 + R_{Co}^3 + R_{Ni}^3\right)\Big/4 + R_O^3\right] \times Z}{3V} \tag{11}$$

where the R denotes the ionic radius related to six coordination number, the V represents the unit cell volume, and Z denotes the unit cell molecular number ($Z = 8$). The packing fraction is detailed in **Table S9**. Fig. 10**(b)** presents the packing fraction of high-entropy $Li_x(MgZnCoNi)_{(1-x)/4}Al_2O_{4-\delta}$ ceramics. A high packing fraction compresses the lattice vibrational space, which efficiently suppresses the lattice vibrations, thus reducing the intrinsic losses and enhancing the $Q \times f$ values [67]. Besides, the trend of the $Q \times f$ values correspond well with that of packing fraction and relative density as the increasing ΔS_{config} (see Fig. 10**(b)**). This indicates that the ΔS_{config} affects the structural evolution and densification of high-entropy $Li_x(MgZnCoNi)_{(1-x)/4}Al_2O_{4-\delta}$ ceramics, and thus has a substantial impact on the $Q \times f$ values.

Moreover, analyzing the FWHM of Raman spectra provides insight into the impact of lattice vibrations on intrinsic loss. The FWHM directly reflects the phonon lifetime, and a longer lifetime decreases the likelihood of coupling with other phonons [50], which results in weaker nonharmonic vibrations and lower damping behavior [68]. This also provides an effective way to study the inherent connection among the ΔS_{config}, lattice vibrations, and $Q \times f$ values. Furthermore, the FWHM is closely related to the damping coefficient, which can be expressed [68]:

$$FWHM = \frac{\gamma\sqrt{\gamma^2 + 4\omega_0^2}}{2\omega_0} \tag{12}$$

$$\tan\sigma = \frac{\gamma\omega_0}{\omega_T^2} \tag{13}$$

where, the γ represents the damping coefficient, and ω_0 and ω_T denote the center frequency of phonon mode and transverse frequency, respectively. The FWHM of the E_g Raman mode are presented in **Table S9**. Fig. 10**(c)** illustrates that the $Q \times f$ value is inversely correlated with the FWHM of E_g Raman mode varying with ΔS_{config} [69]. The lower FWHM implies that the E_g phonon modes interact less with other phonons and the damping behavior of the asymmetric bending of within the [MO_4] tetrahedron is weakened, which leads to a lower intrinsic loss. Additionally, the FWHM of E_g Raman mode exhibits an uptrend trend as ΔS_{config} increases, particularly at ΔS_{config} values of 1.515 R and 1.572 R. This is attributed to the disorderly arrangement of M cations, which disrupts the periodic arrangement of charges, alters ionic polarizabilities, leading to the deterioration of the $Q \times f$ values [70]. Hence, the ΔS_{config} influences the damping behavior of lattice vibrations, thus significantly affecting the $Q \times f$ value.

Furthermore, the $Q \times f$ value is closely linked to the internal fluctuation/strain of d-spacing (η). This can be determined using Stokes and Wilson's formula [53]:

$$\eta = \frac{\beta}{2 \cdot \tan\theta} \tag{14}$$

where β represents the FWHM of the strongest peak (311 plane) in the XRD patterns, and θ denotes the diffraction angle. The measured η is listed in **Table S9**. As the ΔS_{config} increases, the internal fluctuation/strain of high-entropy $Li_x(MgZnCoNi)_{(1-x)/4}Al_2O_{4-\delta}$ ceramics generally shows an upward trend, which contrary to the trend of the $Q \times f$ value (see Fig. 10**(d)**). As the ΔS_{config} decreases (the Li^+ ion content increases), the $Q \times f$ exhibits an overall ascending trend. Since slight disorder is more favorable for stabilizing the strained structure, and a moderate level of oxygen vacancy defects could alleviate the internal fluctuation/strain [53,71]. Evidently, the sample with the least internal fluctuation/strain possesses the highest $Q \times f$ value. Overall, the low configurational entropy corresponds to the low internal strain/fluctuation, which favors structural stability and effectively reduces the anharmonicity of lattice vibrations, thereby enhancing the $Q \times f$ values [52,53,72].

3.4.3. *Temperature coefficient of resonance frequency (τ_f)*

The summary of the τ_f value versus ε_r value in the present study and other high-entropy ceramics are displayed in Fig. 11**(a)**. In comparison to other high-entropy ceramics, high-entropy $Li_x(MgZnCoNi)_{(1-x)/4}Al_2O_{4-\delta}$ ceramics for $x = 0.05$ sample obtained a more near-zero τ_f value (−14 ppm/°C), while possessing a lower ε_r value ($\varepsilon_r = 5.46$). Moreover, as summarized in **Table S10** (see Fig. 11**(a)**), some of the high-entropy ceramics also exhibit near-zero τ_f value. Thus, high-entropy strategy shows great potential for improving the τ_f value. Notably, compared

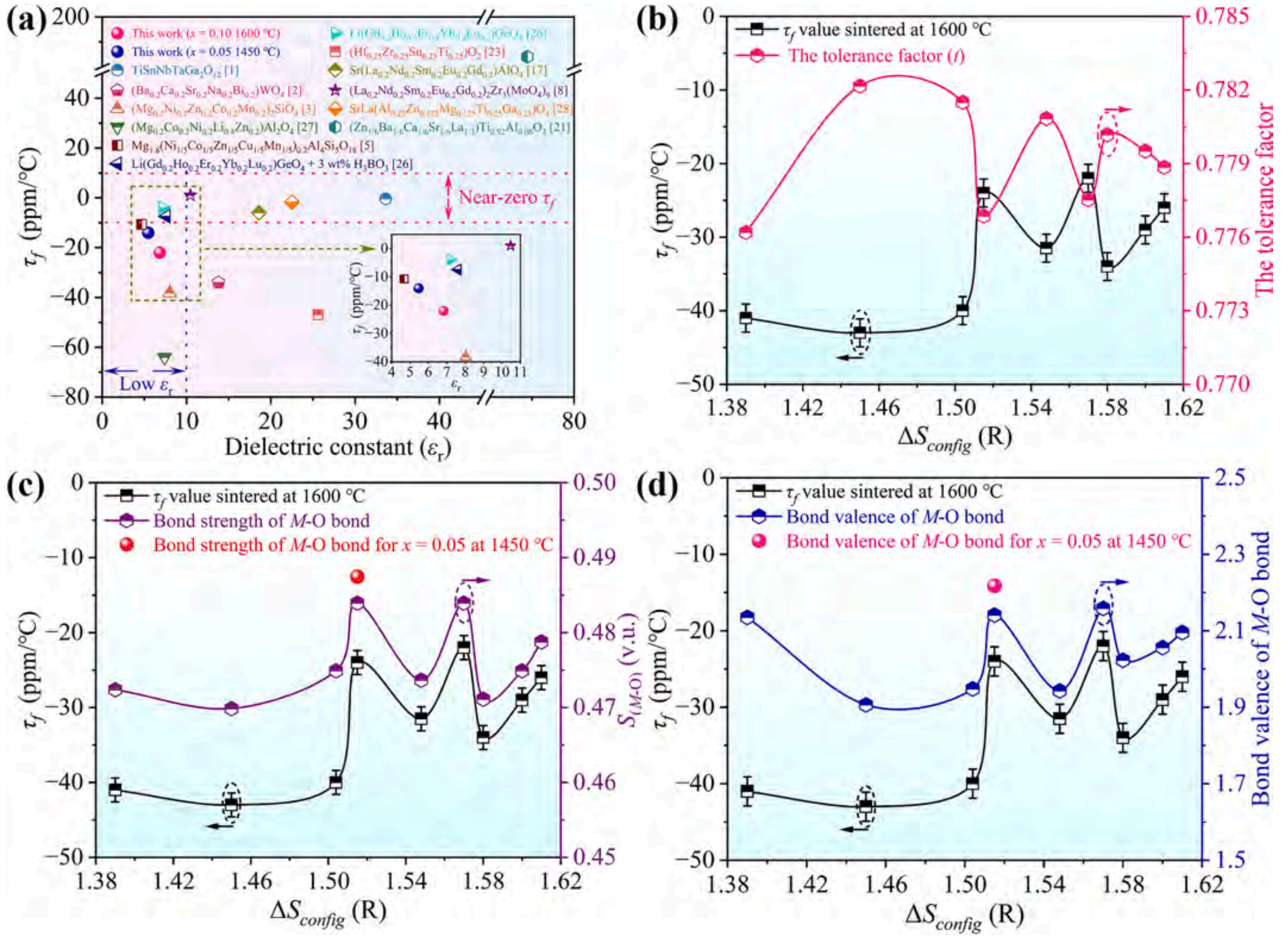

Fig. 11. The τ_f values of high-entropy $Li_x(MgZnCoNi)_{(1\text{-}x)/4}Al_2O_{4\text{-}\delta}$ ceramics for $x = 0.45$ samples sintered at 1600 °C. (a) Summary of the τ_f values versus ε_r values in the present study and other high-entropy ceramics; (b) The τ_f values and tolerance factors; (c) The τ_f values and bond strength of *M*-O bond; (d) The τ_f values and bond valence of *M*-O bond.

with the $MgAl_2O_4$-based ceramics, the τ_f values of the $x = 0.05$ and 0.10 samples of high-entropy $Li_x(MgZnCoNi)_{(1\text{-}x)/4}Al_2O_{4\text{-}\delta}$ ceramics are more near-zero and improve the τ_f value of $MgAl_2O_4$ ceramics ($\tau_f = -75$ ppm/°C) by almost 50 ppm/°C (see **Fig. S4** in *Supplementary Material*).

Fig. 11**(b)** displays the trend of τ_f value with the ΔS_{config} in high-entropy $Li_x(MgZnCoNi)_{(1\text{-}x)/4}Al_2O_{4\text{-}\delta}$ ceramics at 1600 °C. Obviously, τ_f value increases from −43 ppm/°C at 1.450 R to −26 ppm/°C at 1.609 R, which indicates that τ_f value is deeply related to the ΔS_{config}. Notably, the structural stability of ceramic materials is associated with the degree of octahedral distortion. This can be evaluated using the tolerance factor (*t*) as follows [73]:

$$t = \frac{\left[xR_{Li^+} + (1-x)\left(R_{Mg^{2+}} + R_{Zn^{2+}} + R_{Co^{2+}} + R_{Ni^{2+}}\right)/4\right] + R_{O^{2-}}}{\sqrt{2}\left(R_{Al^{3+}} + R_{O^{2-}}\right)} \tag{15}$$

where the R^{+}_{Li}, R^{2+}_{Mg}, R^{2+}_{Zn}, R^{2+}_{Co}, R^{2+}_{Ni}, R^{3+}_{Al}, and R^{2-}_{O} denote the ionic radius of Li^+, Mg^{2+}, Zn^{2+}, Co^{2+}, Ni^{2+}, Al^{3+}, and O^{2-}, respectively. The tolerance factor of high-entropy $Li_x(MgZnCoNi)_{(1\text{-}x)/4}Al_2O_{4\text{-}\delta}$ ceramics is detailed in **Table S11**. Fig. 11**(b)** demonstrates that the overall trend of the tolerance factor decreases gradually as the increasing ΔS_{config}. A lower tolerance factor means that the degree of octahedral distortion is smaller, and the ceramic crystal structure is more stable, which leads to a more near-zero τ_f value [21]. Moreover, the relatively high ΔS_{config} value corresponds well with low tolerance factor, indicating that the stability of high-entropy $Li_x(MgZnCoNi)_{(1\text{-}x)/4}Al_2O_{4\text{-}\delta}$ ceramic structure is favored by relatively high conformational entropy. Notably, the *M*-site elements in high-entropy $Li_x(MgZnCoNi)_{(1\text{-}x)/4}Al_2O_{4\text{-}\delta}$ ceramics exhibit closely matched atomic radius (Mg^{2+}, Zn^{2+}, Li^+, Co^{2+}, and Ni^{2+} are 0.72 Å, 0.74 Å, 0.76 Å, 0.745 Å, and 0.69 Å, respectively). This minimal atomic-size variance can mitigate lattice distortion, enhancing the overall stability the of the ceramic system's internal structure [14,74].

To deeply investigate the intrinsic connection between the ΔS_{config} and τ_f values in high-entropy $Li_x(MgZnCoNi)_{(1\text{-}x)/4}Al_2O_{4\text{-}\delta}$ ceramics, it is vital to discuss the effect of ΔS_{config} on the bond characteristics. Typically, the τ_f relies on the linear thermal expansion coefficient (α_L) and temperature coefficient of the dielectric constant (τ_ε) [35]:

$$\tau_f = -\left(\frac{1}{2}\tau_\varepsilon + \alpha_L\right) \tag{16}$$

Here, the α_L is a constant ($\alpha_L \approx 10$ ppm/°C) within the ceramic materials and remains unaffected by temperature [35]. Thus, the τ_ε plays a leading role in the τ_f. Based on Clausius−Mosotti equation, the τ_ε can be calculated [75]:

$$\begin{aligned}\tau_\varepsilon &= \frac{(\varepsilon-1)(\varepsilon+2)}{3\varepsilon}\left[\frac{1}{\alpha_m}\left(\frac{\partial\alpha_m}{\partial T}\right)_V + \frac{1}{V}\left(\frac{\partial\alpha_m}{\partial T}\right)_T\left(\frac{\partial V}{\partial T}\right)_p - \frac{1}{V}\left(\frac{\partial V}{\partial T}\right)_p\right] \\ &= \frac{(\varepsilon-1)(\varepsilon+2)}{3\varepsilon}(A+B+C)\end{aligned} \tag{17}$$

where the V and α_m represent the volume and polarizability, respectively. Notably, the B and C are parameters connected with the volume expansion, they possess nearly the same magnitude but opposite in sign. Accordingly, the sum of B and C is roughly equivalent to zero, and B and C have a negligible effect on τ_ε [76]. Hence, the τ_ε value is principally dictated by A. Commonly, the term A is associated with the restoring force correlated to the structural parameters of ceramic materials, such as bond strength and bond valence [77]. In the present study, the bond strength ($S_{M\text{–}O}$) and bond valence of M-O bond in high-entropy $Li_x(MgZnCoNi)_{(1-x)/4}Al_2O_{4-\delta}$ ceramics were evaluated [64,65,78]:

$$S = \sum s_0 (R_i/R_0)^{-N} \quad (18)$$

$$V_i = \sum_j v_{ij} \quad (19)$$

$$v_{ij} = \exp\left(\frac{R_{ij} - d_{ij}}{b}\right) \quad (20)$$

where the R_i denote the average bond length between the O anions and M cations, the N and R_0 represent the empirical constants that are contingent on the cation–anion pair and cation site. Moreover, the R_{ij}, d_{ij}, and b signifies the bond valence parameter, the average bond length between i and j atoms, and the universal constant (0.37 Å) [78], respectively. The bond strength and valence of M-O bond in high-entropy $Li_x(MgZnCoNi)_{(1-x)/4}Al_2O_{4-\delta}$ ceramics are detailed in **Tables S12 and S13**.

Normally, the more robust the bond strength, the larger the restoring force to recover the tilted oxygen polyhedron [60]. Hence, an enhancement in the bond strength of M-O bond will lead to a decrease in oxygen polyhedral distortion. Moreover, a higher bond valence means that the bond energy demanded to recover the oxygen polyhedral distortion is increased, resulting in a more stable structure and enhanced thermal stability of the ceramic material [35,50]. As exhibited in Fig. 11 **(c) and (d)**, the bond strength and valence of M-O bond show an upward trend along with increasing ΔS_{config}, indicating that the stability of the oxygen polyhedron is enhanced. This also coincides well with the trend of the τ_f value approaching near-zero. Notably, the bond valence of some samples in present spinel high-entropy ceramic is higher than the theoretical value (2.0 *v.u*), which indicates that the M ions are firmly anchored in the compression site of the cubic [79]. Moreover, the continued rise in M-O bond valence also indicates that the M ions are rattling, and this effect has persisted, which consistent well with the reduction in the ε_r value as discussed above.

Moreover, the $x = 0.05$ samples possess a more near-zero τ_f value (-14 ppm/°C) compared to the others as discussed above (see Fig. 7**(d)**). This can be ascribed to that the bond strength and valence for $x = 0.05$ sample are higher than those of the others. Furthermore, the increase in M-O bond strength also means that the M-O bond length is shortened, the rattling effect is more prominent, and the ionic polarizability becomes weaker, which also leads to the reduction in ε_r value [27,80]. This also agree with the overall decreasing trend of the ε_r value as previously mentioned. In summary, the relatively high conformational entropy contributes to the stability of oxygen polyhedral structure by improving the M-O bond strength and valence in high-entropy $Li_x(MgZnCoNi)_{(1-x)/4}Al_2O_{4-\delta}$ ceramics.

4. Conclusions

In present study, high-entropy $Li_x(MgZnCoNi)_{(1-x)/4}Al_2O_{4-\delta}$ ceramics with spinel structure were prepared using a solid-state reaction route. The internal connection among the ΔS_{config}, structure, and microwave dielectric properties in high-entropy $Li_x(MgZnCoNi)_{(1-x)/4}Al_2O_{4-\delta}$ ceramics was systematically studied. The decrease in cell volume and lattice parameters was assigned to the compression of $[M/AlO_4]$ and/or $[M/AlO_6]$ polyhedron. Receptor Li^+ ions promoted the grain growth and improved the densification of ceramics. The introduction of oxygen vacancy facilitated the Al^{3+} ions to preferentially occupy $[MO_4]$ tetrahedral sites, which increases the covalency and thus improves the $Q\times f$ values. Notably, relatively high conformational entropy increased the phonon vibrational energy and bond strength, which contributes to obtain lower ε_r values. Relatively low conformational entropy corresponded well with the high packing fraction, the suppressed damping behavior, the low internal strain/fluctuation, and high covalency, which reduces the intrinsic losses of non-harmonic vibrations and thus improves the $Q\times f$ values. Moreover, relatively high conformational entropy matched well with low tolerance factor and conduced to the structural stability by enhancing the M-O bond strength and valence, which contributes to achieve near-zero τ_f values. This study demonstrates the effectiveness of adopting high-entropy strategy to modulate the microwave dielectric properties. This research in high-entropy engineering and the presented results are expected to provide crucial theoretical and empirical guidance for achieving superior microwave dielectric properties, thereby fostering the progression of the field.

CRediT authorship contribution statement

Mingjun Xie: Writing – original draft, Formal analysis. **Yuanming Lai:** Writing – review & editing, Supervision, Conceptualization. **Pingwen Xiang:** Writing – review & editing. **Feng Liu:** Data curation. **Linqiao Zhang:** Investigation. **Xingyue Liao:** Validation. **Huan Huang:** Visualization. **Qian Liu:** Funding acquisition. **Chongshen Wu:** Resources. **Yuanxun Li:** Resources.

Declaration of competing interest

The authors declare that they have no known competing financial interests or personal relationships that could have appeared to influence the work reported in this paper.

Data availability

The authors are unable or have chosen not to specify which data has been used.

Acknowledgements

This research was funded by the Sichuan Science and Technology Program (No. 2023YFQ0082). Guangdong Provincial Key Laboratory of Electronic Functional Materials and Devices, grant number EFMD2022005Z. Chengdu Science and Technology Program (No. 2023-GH02-00061-HZ).

Appendix A. Supplementary material

Supplementary data to this article can be found online at https://doi.org/10.1016/j.cej.2024.154132.

References

[1] L. Xiao, L. Deng, Y. Li, Z. Qing, Y. Xi, J. Zhu, S. Peng, A $TiSnNbTaGa_2O_{12}$ high-entropy microwave dielectric ceramic with rutile structure and near-zero τ_f, J. Eur. Ceram. Soc. 44 (2023) 277–283, https://doi.org/10.1016/j.jeurceramsoc.2023.08.031.

[2] P. Shao, X. Lyu, Q. Sun, Z. Lang, J. Wang, R. Li, L. Xin, X. Luo, P. Lyu, L. Ren, M. Zhang, Synthesis, microstructure, and dielectric properties of novel dual-phase high-entropy $(Ba_{0.2}Ca_{0.2}Sr_{0.2}Na_{0.2}Bi_{0.2})WO_4$ ceramics for LTCC applications, J. Eur. Ceram. Soc. 44 (2024) 5203–5210, https://doi.org/10.1016/j.jeurceramsoc.2024.02.046.

[3] K. Liu, H. Zhang, C. Liu, J. Li, L. Shi, X. Wang, D. Zhang, Crystal structure and microwave dielectric properties of $(Mg_{0.2}Ni_{0.2}Zn_{0.2}Co_{0.2}Mn_{0.2})_2SiO_4$ - A novel high-entropy ceramic, Ceram. Int. 48 (2022) 23307–23313, https://doi.org/10.1016/j.ceramint.2022.04.317.

[4] F. Li, Y. Li, S. Li, Y. Luo, Y. Lu, T. Tang, Y. Liao, J. Zhang, Q. Wen, All-ceramic array patch for 5G signal enhancement based on B-site substituted zinc-cobalt molybdate

low temperature co-fired ceramics, Chem. Eng. J. 466 (2023) 143325, https://doi.org/10.1016/j.cej.2023.143325.

[5] Y. Yao, L. Cao, H. Yang, R. Muhammad, Y. Ren, X. Luo, F. Hussain, B. Liu, M. Mao, H.B. Bafrooei, E. Taheri-Nassaj, K. Song, High-entropy $Mg_{1.8}R_{0.2}Al_4Si_5O_{18}$ (R = Ni Co, Zn, Cu, Mn) cordierite ceramics: Influence of octahedral distortion and electronegativity mismatch on the microwave dielectric properties, Ceram. Int. 18 (2024) 2–7, https://doi.org/10.1016/j.ceramint.2024.02.215.

[6] H. Tian, J. Zheng, L. Liu, H. Wu, H. Kimura, Y. Lu, Z. Yue, Structure characteristics and microwave dielectric properties of $Pr_2(Zr_{1-x}Ti_x)_3(MoO_4)_9$ solid solution ceramic with a stable temperature coefficient, J. Mater. Sci. Technol. 116 (2022) 121–129, https://doi.org/10.1016/j.jmst.2021.10.051.

[7] J. Bao, Y. Zhang, H. Kimura, H. Wu, Z. Yue, Crystal structure, chemical bond characteristics, infrared reflection spectrum, and microwave dielectric properties of $Nd_2(Zr_{1-x}Ti_x)_3(MoO_4)_9$ ceramics, J. Adv. Ceram. 12 (2023) 82–92, https://doi.org/10.26599/JAC.2023.9220668.

[8] H. Tian, X. Zhang, W. Du, Z. Feng, L. Wang, H. Wu, W. Xia, Structure characteristics and microwave/terahertz dielectric response of low-permittivity $(La_{0.2}Nd_{0.2}Sm_{0.2}Eu_{0.2}Gd_{0.2})_2Zr_3(MoO_4)_9$ high-entropy ceramics, Ceram. Int. 50 (2024) 6403–6411, https://doi.org/10.1016/j.ceramint.2023.11.378.

[9] Y. Lai, X. Tang, X. Huang, H. Zhang, X. Liang, J. Li, H. Su, Phase composition, crystal structure and microwave dielectric properties of $Mg_{2-x}Cu_xSiO_4$ ceramics, J. Eur. Ceram. Soc. 38 (2018) 1508–1516, https://doi.org/10.1016/j.jeurceramsoc.2017.10.035.

[10] Z. Wang, J. Chen, H. Xiang, L. Fang, Structural and chemical bond characteristics of microwave dielectric ceramics $Sm_{3-x}Bi_xGa_5O_{12}$, Ceram. Int. 48 (2022) 18723–18729, https://doi.org/10.1016/j.ceramint.2022.03.146.

[11] X. Chen, H. Li, P. Zhang, H. Hu, G. Chen, G. Li, A low-permittivity microwave dielectric ceramic $BaZnP_2O_7$ and its performance modification, J. Am. Ceram. Soc. 104 (2021) 5214–5223, https://doi.org/10.1111/jace.17839.

[12] S.S. Sohn, A. Kwiatkowski da Silva, Y. Ikeda, F. Körmann, W. Lu, W.S. Choi, B. Gault, D. Ponge, J. Neugebauer, D. Raabe, Ultrastrong Medium-Entropy Single-Phase Alloys Designed via Severe Lattice Distortion, Adv. Mater. 31 (2019) 1–8, https://doi.org/10.1002/adma.201807142.

[13] J.W. Bae, J.B. Seol, J. Moon, S.S. Sohn, M.J. Jang, H.Y. Um, B.J. Lee, H.S. Kim, Exceptional phase-transformation strengthening of ferrous medium-entropy alloys at cryogenic temperatures, Acta Mater. 161 (2018) 388–399, https://doi.org/10.1016/j.actamat.2018.09.057.

[14] M. Zhang, X. Xu, S. Ahmed, Y. Yue, M. Palma, P. Svec, F. Gao, I. Abrahams, M. J. Reece, H. Yan, Phase transformations in an Aurivillius layer structured ferroelectric designed using the high entropy concept, Acta Mater. 229 (2022) 117815, https://doi.org/10.1016/j.actamat.2022.117815.

[15] D. Bérardan, S. Franger, A.K. Meena, N. Dragoe, Room temperature lithium superionic conductivity in high entropy oxides, J. Mater. Chem. A 4 (2016) 9536–9541, https://doi.org/10.1039/c6ta03249d.

[16] D. Bérardan, S. Franger, D. Dragoe, A.K. Meena, N. Dragoe, Colossal dielectric constant in high entropy oxides, Phys. Status Solidi - Rapid Res. Lett. 10 (2016) 328–333, https://doi.org/10.1002/pssr.201600043.

[17] F.L. Lin, B. Liu, C.C. Hu, K.X. Song, Novel high-entropy microwave dielectric ceramics $Sr(La_{0.2}Nd_{0.2}Sm_{0.2}Eu_{0.2}Gd_{0.2})AlO_4$ with excellent temperature stability and mechanical properties, J. Eur. Ceram. Soc. 43 (2023) 2506–2512, https://doi.org/10.1016/j.jeurceramsoc.2023.01.028.

[18] P. Zhang, L. Gong, X. Xu, Z. Lou, Z. Wei, P. Chen, Z. Wu, J. Xu, F. Gao, Thermoelectric enhancement in A-site deficient high-entropy perovskite $(Sr_{0.25}Ca_{0.25}La_{0.25}Ba_{0.25})_{1-x}TiO_{3\pm\delta}$ ceramics by fine manipulating cation vacancies, Chem. Eng. J. 472 (2023) 144974, https://doi.org/10.1016/j.cej.2023.144974.

[19] J. Liu, C. Ma, R. Liang, X. Zhao, Y. Bai, X. Liu, K. Ren, H. Du, Y. Wang, Phase transition and large strain response with ultra-low hysteresis of $BaTiO_3$ doped with a high-entropy perovskite oxide, Chem. Eng. J. 488 (2024) 150823, https://doi.org/10.1016/j.cej.2024.150823.

[20] B. Yan, K. Chen, L. An, Design and preparation of lead-free $(Bi_{0.4}Na_{0.2}K_{0.2}Ba_{0.2})TiO_3$-$Sr(Mg_{1/3}Nb_{2/3})O_3$ high-entropy relaxor ceramics for dielectric energy storage, Chem. Eng. J. 453 (2023) 139921, https://doi.org/10.1016/j.cej.2022.139921.

[21] T. Su, H. Chen, Z. Wei, M. Hao, X. Wang, Y. Liu, C. Ma, Y. Miao, F. Gao, Structure and microwave dielectric properties of Al^{3+}-doped $(Zn_{1/6}Ba_{1/6}Ca_{1/6}Sr_{1/6}La_{1/3})TiO_3$ high-entropy ceramics system, Ceram. Int. 50 (2024) 5043–5051, https://doi.org/10.1016/j.ceramint.2023.11.249.

[22] J.W. Yeh, Recent progress in high-entropy alloys, Ann. Chim. Sci. Des Mater. 31 (2006) 633–648, https://doi.org/10.3166/acsm.31.633-648.

[23] Y.H. Ding, L. Liu, R.Z. Guo, L. Li, X.M. Chen, $(Hf_{0.25}Zr_{0.25}Sn_{0.25}Ti_{0.25})O_2$ high-entropy ceramics and their microwave dielectric characteristics, J. Am. Ceram. Soc. 105 (2022) 6710–6717, https://doi.org/10.1111/jace.18641.

[24] H. Zhao, W. Cao, C. Liang, C. Wang, C. Wang, Lead-free medium-entropy $(Na_{0.47(1-x)}Bi_{0.47(1-x)}Ba_{0.06(1-x)}Sr_{0.7x}Nd_{0.2x})TiO_3$ relaxor ceramics with robust energy-storage performance, Chem. Eng. J. 471 (2023) 144702, https://doi.org/10.1016/j.cej.2023.144702.

[25] Z. Wang, R. Kang, L. Zhang, X. Lou, Y. Zhao, P. Mao, J. Wang, Ultrahigh energy-storage capacity achieved in $(Bi_{0.5}Na_{0.5})TiO_3$-based high-entropy dielectric capacitors with linear-like polarization response, Chem. Eng. J. 474 (2023) 145506, https://doi.org/10.1016/j.cej.2023.145506.

[26] H. Xiang, L. Yao, J. Chen, A. Yang, H. Yang, L. Fang, Microwave dielectric high-entropy ceramic $Li(Gd_{0.2}Ho_{0.2}Er_{0.2}Yb_{0.2}Lu_{0.2})GeO_4$ with stable temperature coefficient for low-temperature cofired ceramic technologies, J. Mater. Sci. Technol. 93 (2021) 28–32, https://doi.org/10.1016/j.jmst.2021.03.057.

[27] M. Xie, X. Li, Y. Lai, C. Qi, J. Yin, W. Gong, Y. Li, Q. Liu, C. Wu, Phase evolution and microware dielectric properties of high-entropy spinel-type $(Mg_{0.2}Co_{0.2}Ni_{0.2}Li_{0.4}Zn_{0.2})Al_2O_4$ ceramics, J. Eur. Ceram. Soc. 44 (2023) 284–292, https://doi.org/10.1016/j.jeurceramsoc.2023.09.017.

[28] F.L. Lin, B. Liu, Q.W. Zhou, Y.H. Cheng, K.X. Song, Novel non-equimolar SrLa $(Al_{0.25}Zn_{0.125}Mg_{0.125}Ga_{0.25}Ti_{0.25})O_4$ high-entropy ceramics with excellent mechanical and microwave dielectric properties, J. Eur. Ceram. Soc. 43 (2023) 6909–6915, https://doi.org/10.1016/j.jeurceramsoc.2023.07.072.

[29] S. Zhou, Y. Pu, Q. Zhang, R. Shi, X. Guo, W. Wang, J. Ji, T. Wei, T. Ouyang, Microstructure and dielectric properties of high entropy Ba $(Zr_{0.2}Ti_{0.2}Sn_{0.2}Hf_{0.2}Me_{0.2})O_3$ perovskite oxides, Ceram. Int. 46 (2020) 7430–7437, https://doi.org/10.1016/j.ceramint.2019.11.239.

[30] J. Rodríguez-Carvajal, Recent advances in magnetic structure determination by neutron powder diffraction, Phys. B Phys. Condens. Matter 192 (1993) 55–69, https://doi.org/10.1016/0921-4526(93)90108-I.

[31] L. Xiang, A.K. Darboe, Z. Luo, X. Qi, J. jing Shao, X.J. Ye, C.S. Liu, K. Sun, Y. Qu, J. Xu, W. Zhong, Constructing two-dimensional/two-dimensional reduced graphene oxide/MoX_2 (X = Se and S) van der Waals heterojunctions: a combined composition modulation and interface engineering strategy for microwave absorption, Adv. Compos. Hybrid Mater. 6 (2023) 1–15, https://doi.org/10.1007/s42114-023-00793-3.

[32] S. Akrami, P. Edalati, M. Fuji, K. Edalati, High-entropy ceramics: Review of principles, production and applications, Mater. Sci. Eng. R Reports 146 (2021) 100644, https://doi.org/10.1016/j.mser.2021.100644.

[33] H. Yang, S. Zhang, H. Yang, Y. Yuan, E. Li, Influence of $(Al_{1/3}W_{2/3})^{5+}$ co-substitution for Nb^{5+} in $NdNbO_4$ and the impact on the crystal structure and microwave dielectric properties, Dalt. Trans. 47 (2018) 15808–15815, https://doi.org/10.1039/c8dt03134g.

[34] V. D`Ippolito, G.B. Andreozzi, D. Bersani, P.P. Lottici, Raman fingerprint of chromate, aluminate and ferrite spinels, J. Raman Spectrosc. 46 (2015) 1255–1264, https://doi.org/10.1002/jrs.4764.

[35] X. Wei, Y. He, X. Chen, H. Zhou, Phase Composition, Raman Spectrum and Microwave Dielectric Properties of glass-free low temperature co-fired ACaPr $(MoO_4)_3$ (A = Na, K) Ceramics, Ceram. Int. 49 (2023) 36962–36969, https://doi.org/10.1016/j.ceramint.2023.09.028.

[36] Y. Ding, C.C. Hu, W.Q. Sheng, K.X. Song, B. Liu, Crystal structure, microwave dielectric properties, and dielectric resonant antenna studies of novel low-permittivity $CoAl_2O_4$ spinel ceramics, J. Mater. Sci. Mater. Electron. 32 (2021) 22813–22821, https://doi.org/10.1007/s10854-021-06760-2.

[37] C.M. Álvarez-Docio, J.J. Reinosa, A. Del Campo, J.F. Fernández, Investigation of thermal stability of 2D and 3D $CoAl_2O_4$ particles in core-shell nanostructures by Raman spectroscopy, J. Alloys Compd. 779 (2019) 244–254, https://doi.org/10.1016/j.jallcom.2018.11.263.

[38] T. Qin, C. Zhong, Y. Qin, B. Tang, S. Zhang, The structure evolution and microwave dielectric properties of $MgAl_{2-x}(Mg_{0.5}Ti_{0.5})_xO_4$ solid solutions, Ceram. Int. 46 (2020) 19046–19051, https://doi.org/10.1016/j.ceramint.2020.04.236.

[39] T. Qin, C. Zhong, Y. Shang, L. Cao, M. Wang, B. Tang, S. Zhang, Effects of LiF on crystal structure, cation distributions and microwave dielectric properties of $MgAl_2O_4$, J. Alloys Compd. 886 (2021) 161278, https://doi.org/10.1016/j.jallcom.2021.161278.

[40] T.F.C. and M.N. H. Cynn, S.K. Sharma, High-temperature Raman investigation of order-disorder behavior in the $MgA1_2O_4$ spinel, Phys. Rev. B 45 (1992) 500–502.

[41] S. Takahashi, A. Kan, H. Ogawa, Microwave dielectric properties and crystal structures of spinel-structured $MgAl_2O_4$ ceramics synthesized by a molten-salt method, J. Eur. Ceram. Soc. 37 (2017) 1001–1006, https://doi.org/10.1016/j.jeurceramsoc.2016.10.018.

[42] D. Zhou, L.X. Pang, H. Wang, J. Guo, X. Yao, C.A. Randall, Phase transition, Raman spectra, infrared spectra, band gap and microwave dielectric properties of low temperature firing $(Na_{0.5x}Bi_{1-0.5x})$ $(Mo_xV_{1-x})O_4$ solid solution ceramics with scheelite structures, J. Mater. Chem. 21 (2011) 18412–18420, https://doi.org/10.1039/c1jm14004c.

[43] S.W. Seo, M.W. Park, J.S. Lee, Effects of lithium oxide addition on sintering behavior and electrical conductivity of $Ce_{0.8}Gd_{0.2}O$ ceramics prepared by commercial powders, J. Nanosci. Nanotechnol. 16 (2016) 5320–5323, https://doi.org/10.1166/jnn.2016.12272.

[44] X. Zhong, M. He, C. Zhang, Y. Guo, J. Hu, J. Gu, Heterostructured BN@Co-C@C Endowing Polyester Composites Excellent Thermal Conductivity and Microwave Absorption at C Band, Adv. Funct. Mater. 34 (2024) 1–13, https://doi.org/10.1002/adfm.202313544.

[45] X. Yang, Y. Lai, Y. Zeng, F. Yang, F. Huang, B. Li, F. Wang, C. Wu, H. Su, Spinel-type solid solution ceramic $MgAl_2O_4$-Mg_2TiO_4 with excellent microwave dielectric properties, J. Alloys Compd. 898 (2022) 162905, https://doi.org/10.1016/j.jallcom.2021.162905.

[46] F. Yang, Y. Lai, Y. Zeng, Q. Zhang, J. Han, X. Zhong, H. Su, Ultra-high quality factor and low dielectric constant of $(Zn_{0.5}Ti_{0.5})^{3+}$ co-substituted $MgAl_2O_4$ ceramic, Ceram. Int. 47 (2021) 22522–22529, https://doi.org/10.1016/j.ceramint.2021.04.261.

[47] S.D. Ramarao, V.R.K. Murthy, Crystal structure refinement and microwave dielectric properties of new low dielectric loss $AZrNb_2O_8$ (A: Mn, Zn, Mg and Co) ceramics, Scr. Mater. 69 (2013) 274–277, https://doi.org/10.1016/j.scriptamat.2013.04.018.

[48] Y. Lai, H. Su, G. Wang, X. Tang, X. Liang, X. Huang, Y. Li, H. Zhang, C. Ye, X. R. Wang, Improved microwave dielectric properties of $CaMgSi_2O_6$ ceramics through CuO doping, J. Alloys Compd. 772 (2019) 40–48, https://doi.org/10.1016/j.jallcom.2018.09.059.

[49] R.D. Shannon, Dielectric polarizabilities of ions in oxides and fluorides, J. Appl. Phys. 73 (1993) 348–366, https://doi.org/10.1063/1.353856.

[50] M. Zhou, H. Chen, G. Zhou, Y. He, S. Zhang, B. Tang, Co-effects of Nb_2O_5 and stoichiometric deviations on the microwave dielectric properties of $Y_3Al_5O_{12}$, Ceram. Int. 48 (2022) 18651–18657, https://doi.org/10.1016/j.ceramint.2022.03.137.

[51] A. Das Arulsamy, Renormalization group method based on the ionization energy theory, Ann. Phys. (N. Y). 326 (2011) 541–565, https://doi.org/10.1016/j.aop.2010.09.011.

[52] L. Li, Y. Li, J. Qiao, M. Du, Developing high-Q×f value $MgNb_{2-x}Ta_xO_6$ ($0 \le x \le 0.8$) columbite ceramics and clarifying the impact mechanism of dielectric loss: Crystal structure, Raman vibrations, microstructure, lattice defects, chemical bond characteristics, structural parameters, and mi crowave dielectric properties in-depth studies, J. Mater. Sci. Technol. 146 (2023) 186–199, https://doi.org/10.1016/j.jmst.2022.10.061.

[53] X. Zhang, Z. Fang, H. Yang, P. Zhao, X. Zhang, Y. Li, Z. Xiong, H. Yang, S. Zhang, B. Tang, Lattice evolution, ordering transformation and microwave dielectric properties of rock-salt $Li_{3+x}Mg_{2-2x}Nb_{1-x}Ti_{2x}O_6$ solid-solution system: A newly developed pseudo ternary phase diagram, Acta Mater. 206 (2021) 116636, https://doi.org/10.1016/j.actamat.2021.116636.

[54] W. Liu, Y. Li, X. Liu, Y. Lu, A novel $NaMg_{(1-x)}Zn_x(PO_3)_3$ microwave dielectric ceramic with an ultra-low dielectric constant for LTCC application, Ceram. Int. 50 (2023) 143–149, https://doi.org/10.1016/j.ceramint.2023.10.059.

[55] N. Osenciat, D. Bérardan, D. Dragoe, B. Léridon, S. Holé, A.K. Meena, S. Franger, N. Dragoe, Charge compensation mechanisms in Li-substituted high-entropy oxides and influence on Li superionic conductivity, J. Am. Ceram. Soc. 102 (2019) 6156–6162, https://doi.org/10.1111/jace.16511.

[56] T.F. Zhang, X.G. Tang, Q.X. Liu, Y.P. Jiang, X.X. Huang, Oxygen-vacancy-related high temperature dielectric relaxation in $(Pb_{1-x}Ba_x)ZrO_3$ ceramics, J. Am. Ceram. Soc. 98 (2014) 551–558, https://doi.org/10.1111/jace.13317.

[57] J.J. Zhang, H. Liu, Y. Gu, J.J. Zhang, X. Zhang, X. Qi, Oxygen-vacancy-related dielectric relaxations and electrical properties in $[Li_x(BaSrCaMg)_{(1-x)/4}]TiO_3$ high-entropy perovskite ceramics, J. Mater. Sci. Mater. Electron. 33 (2022) 9918–9929, https://doi.org/10.1007/s10854-022-07982-8.

[58] B. Zhan, Y. Hao, X. Qi, Q. Peng, W. Zhong, Y. Qu, J. Ding, J. Yang, X. Gong, Y. Chen, Multifunctional cellular carbon foams derived from chitosan toward self-cleaning, thermal insulation, and highly efficient microwave absorption properties, Nano Res. 17 (2024) 927–938, https://doi.org/10.1007/s12274-023-6236-7.

[59] J. Xiao, B. Zhan, M. He, X. Qi, X. Gong, J.L. Yang, Y. Qu, J. Ding, W. Zhong, J. Gu, Interfacial Polarization Loss Improvement Induced by the Hollow Engineering of Necklace-like PAN/Carbon Nanofibers for Boosted Microwave Absorption, Adv. Funct. Mater. 2316722 (2024) 1–12, https://doi.org/10.1002/adfm.202316722.

[60] Z. Xiong, C. Yang, B. Tang, Z. Fang, H. Chen, S. Zhang, Structure–property relationships of perovskite-structured $Ca_{0.61}Nd_{0.26}Ti_{1-x}(Cr_{0.5}Nb_{0.5})_xO_3$ ceramics, Ceram. Int. 44 (2018) 7384–7392, https://doi.org/10.1016/j.ceramint.2017.12.186.

[61] B. Ullah, W. Lei, X.H. Wang, G.F. Fan, X.C. Wang, W.Z. Lu, Dielectric and ferroelectric behavior of an incipient ferroelectric $Sr_{(1-3x/2)}Ce_xTiO_3$ novel solid solution, RSC Adv. 6 (2016) 91679–91688, https://doi.org/10.1039/c6ra18717j.

[62] W. Pan, M. Cao, H. Hao, Z. Yao, Z. Yu, H. Liu, Defect engineering toward the structures and dielectric behaviors of (Nb, Zn) co-doped $SrTiO_3$ ceramics, J. Eur. Ceram. Soc. 40 (2020) 49–55, https://doi.org/10.1016/j.jeurceramsoc.2019.09.027.

[63] S. Takahashi, A. Kan, H. Ogawa, Microwave dielectric properties and crystal structures of $Mg_{0.7}Al_{2.2}O_4$ and $Mg_{0.4}Al_{2.4}O_4$ ceramics with defect structures, J. Am. Ceram. Soc. 100 (2017) 3497–3504, https://doi.org/10.1111/jace.14847.

[64] I.D. Brown, K.K. Wu, Empirical parameters for calculating cation–oxygen bond valences, Acta Crystallogr, Sect. B Struct. Crystallogr. Cryst. Chem. 32 (1976) 1957–1959, https://doi.org/10.1107/s0567740876006869.

[65] I.D. Brown, R.D. Shannon, Empirical bond-strength–bond-length curves for oxides, Acta Crystallogr. Sect. A 29 (1973) 266–282, https://doi.org/10.1107/S0567739473000689.

[66] H. Yang, Y. Wang, X. Zhang, M. Xing, E. Li, L. Chai, Crystal structure, phase transition, vibrational spectra, and microwave dielectric characteristics of Ta^{5+} ionic substituted $Co_{0.5}Ti_{0.5}NbO_4$ ceramics, Ceram. Int. 48 (2022) 648–655, https://doi.org/10.1016/j.ceramint.2021.09.144.

[67] L. Liu, J. Du, B. Tao, F. Zhang, H. Wu, Structure, microwave dielectric properties, and infrared reflectivity spectrum of W^{6+} substituted $Ce_2Zr_3(MoO_4)_9$ ceramics, Ceram. Int. 47 (2021) 19142–19152, https://doi.org/10.1016/j.ceramint.2021.03.261.

[68] Z. Wang, Y. Guo, J. Li, Investigation on phase structure, spectral characteristics, microstructure and microwave dielectric properties of $Li_2Zn[Ti_{1-x}(Co_{1/3}Nb_{2/3})_x]_3O_8$ ($0.0 \le x \le 0.4$) ceramics, Ceram. Int. 49 (2023) 15304–15314, https://doi.org/10.1016/j.ceramint.2023.01.114.

[69] Y. Wang, J. Li, W. Fang, Y. Tang, Z. Zhang, H. Xiang, L. Fang, A novel ultra-high Q microwave dielectric ceramic $ZnMgTiO_4$ with spinel structure, Ceram. Int. 49 (2023) 35420–35427, https://doi.org/10.1016/j.ceramint.2023.08.218.

[70] Q. Zhang, L. Xu, X. Tang, F. Huang, X. Wu, Y. Li, Y. Jing, Z.K. Han, H. Su, Electronic structure, Raman spectra, and microwave dielectric properties of Co-substituted $ZnWO_4$ ceramics, J. Alloys Compd. 874 (2021) 159928, https://doi.org/10.1016/j.jallcom.2021.159928.

[71] M. Zhou, H. Chen, X. Zhang, B. Tang, Phase composition, microstructure, and microwave dielectric properties of non-stoichiometric yttrium aluminum garnet ceramics, J. Eur. Ceram. Soc. 42 (2022) 472–477, https://doi.org/10.1016/j.jeurceramsoc.2021.10.040.

[72] Z. Cheng, L. Xu, X. Wang, X. Wu, F. Huang, Y. Jing, H. Su, The effect of B-site ions on crystal structure evolution and microwave dielectric properties of gillespite-type $SrCu_{0.95}B_{0.05}(B^{2+}$: Cu, Co, Mn, Ni, Mg, Zn$)Si_4O_{10}$, Ceram. Int. 49 (2023) 36800–36806, https://doi.org/10.1016/j.ceramint.2023.09.009.

[73] G. Wang, Q. Fu, H. Shi, F. Tian, M. Wang, L. Yan, Z. Zheng, W. Luo, Suppression of oxygen vacancies generation in $Ba_{6-3x}Sm_{8+2x}Ti_{18}O_{54}$ ($x = 2/3$) microwave dielectric ceramics through Pr substitution, Ceram. Int. 45 (2019) 22148–22155, https://doi.org/10.1016/j.ceramint.2019.07.233.

[74] F. Lin, Y. Lai, B. Li, Y. Li, W. Gong, Q. Zhang, M. Xie, C. Wu, Crystal structure and ultra-high quality factor of $MgTi_{1-x}(Co_{1/3}Nb_{2/3})_xO_3$ solid-solution microwave ceramics, Ceram. Int. 49 (2023) 40374–40381, https://doi.org/10.1016/j.ceramint.2023.10.010.

[75] S.D. Rama Rao, S. Roopas Kiran, V.R.K. Murthy, Correlation between structural characteristics and microwave dielectric properties of scheelite $Ca_{1-x}Cd_xMoO_4$ solid solution, J. Am. Ceram. Soc. 95 (2012) 3532–3537, https://doi.org/10.1111/j.1551-2916.2012.05317.x.

[76] A.J. Bosman, E.E. Havinga, Temperature dependence of dielectric constants of cubic ionic compounds, Phys. Rev. 129 (1963) 1593–1600, https://doi.org/10.1103/PhysRev.129.1593.

[77] C. Li, S. Ding, Y. Zhang, H. Zhu, T. Song, Effects of Ni^{2+} substitution on the crystal structure, bond valence, and microwave dielectric properties of $BaAl_{2-2x}Ni_{2x}Si_2O_{8-x}$ ceramics, J. Eur. Ceram. Soc. 41 (2021) 2610–2616, https://doi.org/10.1016/j.jeurceramsoc.2020.12.011.

[78] N.E. Brese, M. O'Keeffe, Bond-valence parameters for solids, Acta Crystallogr. Sect. B 47 (1991) 192–197, https://doi.org/10.1107/S0108768190011041.

[79] J. Wu, H. Xiang, Y. Sun, A. Cao, L. Fang, Effect of heterovalent ion doping on the polarization ability and dielectric loss of fluorite $Ce_{1-x}Y_xO_{1-x/2}$ ceramics in the microwave frequency band, Ceram. Int. 49 (2023) 37712–37719, https://doi.org/10.1016/j.ceramint.2023.09.097.

[80] C. Li, J. Hou, Z. Ye, R. Muhammad, A. Li, M. Ma, G. Wu, K. Song, T. Zhou, M. Mao, B. Liu, H.B. Bafrooei, E. Taheri-nassaj, S. Luo, F. Shi, S. Sun, D. Wang, Lattice occupying sites and microwave dielectric properties of Mg^{2+}–Si^{4+} co-doped $Mg_xY_{3-x}Al_{5-x}Si_xO_{12}$ garnet typed ceramics, J. Mater. Sci. Mater. Electron. 33 (2022) 2116–2124, https://doi.org/10.1007/s10854-021-07417-w.